



Structural basis of siRNA recognition by TRBP double-stranded RNA binding domains

Gregoire Masliah¹, Christophe Maris¹, Sebastian LB König², Maxim Yulikov³, Florian Aeschmann⁴, Anna L Malinowska⁵, Julie Mabile⁴, Jan Weiler⁴, Andrea Holla², Juerg Hunziker⁴, Nicole Meisner-Kober⁴, Benjamin Schuler², Gunnar Jeschke³ & Frederic H-T Allain^{1,*}

Abstract

The accurate cleavage of pre-micro(mi)RNAs by Dicer and mi/siRNA guide strand selection are important steps in forming the RNA-induced silencing complex (RISC). The role of Dicer binding partner TRBP in these processes remains poorly understood. Here, we solved the solution structure of the two N-terminal dsRNA binding domains (dsRBDs) of TRBP in complex with a functionally asymmetric siRNA using NMR, EPR, and single-molecule spectroscopy. We find that siRNA recognition by the dsRBDs is not sequence-specific but rather depends on the RNA shape. The two dsRBDs can swap their binding sites, giving rise to two equally populated, pseudo-symmetrical complexes, showing that TRBP is not a primary sensor of siRNA asymmetry. Using our structure to model a Dicer-TRBP-siRNA ternary complex, we show that TRBP's dsRBDs and Dicer's RNase III domains bind a canonical 19 base pair siRNA on opposite sides, supporting a mechanism whereby TRBP influences Dicer-mediated cleavage accuracy by binding the dsRNA region of the pre-miRNA during Dicer cleavage.

Keywords Dicer; NMR; single-molecule FRET; siRNA; TRBP

Subject Categories RNA Biology; Structural Biology

DOI 10.15252/embj.201797089 | Received 11 April 2017 | Revised 10 January 2018 | Accepted 12 January 2018

The EMBO Journal (2018) e97089

Introduction

RNA interference (RNAi) is a control mechanism of gene expression relying on small non-coding RNAs (Mello & Conte, 2004; Carthew & Sontheimer, 2009). One hallmark of the RNAi pathway is the RNA-induced silencing complex (RISC), a ribonucleoprotein (RNP) comprising the protein Argonaute (Ago) along with a single-stranded RNA of 21–23 nucleotides called microRNA

(miRNA) or short interfering RNA (siRNA) (Sontheimer, 2005). Gene silencing is brought about by the formation of Watson–Crick interactions between the miRNA component of the RISC and cognate mRNAs (Sontheimer, 2005).

miRNA biogenesis is initiated in the nucleus with RNA polymerase II transcribing the primary miRNA (pri-miRNA), a precursor containing one or several stem-loop elements flanked by single-stranded RNA regions (Bartel, 2004; Kim, 2005a,b). The pri-miRNA is processed by the microprocessor, a complex containing the ribonuclease III (RNase III) enzyme Drosha and the RNA-binding protein DGCR8, resulting in the release of the pre-miRNA (Denli *et al.*, 2004; Gregory *et al.*, 2004; Herbert *et al.*, 2016; Kwon *et al.*, 2016). Pre-miRNA secondary structure typically consists of a hairpin of ~70 nucleotides with irregularities such as bulges and internal loops, and a characteristic two-nucleotide overhang at its 3' end. Pre-miRNA is exported through the exportin 5 complex into the cytoplasm (Lund *et al.*, 2004; Kim *et al.*, 2009), where the RNase III enzyme Dicer excises its apical loop, thereby producing a mature miRNA duplex displaying 2-nucleotide overhangs at both 3' ends (Bernstein *et al.*, 2001; Hutvagner *et al.*, 2001). Following the transfer of the miRNA duplex to a member of the Argonaute family, one of the two RNA strands—the “passenger”—is removed from Ago, while the other strand—the “guide”—is retained in the mature RISC particle, a process known as “strand sorting” or “strand selection” (Sontheimer, 2005; Tomari & Zamore, 2005; Kawamata *et al.*, 2009).

The molecular mechanisms governing strand selection are not yet completely understood. Structural studies of Ago in complex with various RNAs have shown that the 5' and 3' ends of the miRNA guide strand are bound to the MID and PAZ domains of Ago (Lingel *et al.*, 2003, 2004; Song *et al.*, 2003; Ma *et al.*, 2004, 2005; Frank *et al.*, 2010). When the miRNA duplex is loaded onto Ago, only the guide strand is retained (Matranga *et al.*, 2005; Rand *et al.*, 2005; Leuschner *et al.*, 2006; Kawamata *et al.*, 2009). The identity of the guide strand is therefore determined by the

1 Institute of Molecular Biology and Biophysics, ETH Zürich, Zürich, Switzerland

2 Department of Biochemistry, University of Zürich, Zürich, Switzerland

3 Laboratory of Physical Chemistry, ETH Zürich, Zürich, Switzerland

4 Novartis Institutes for Biomedical Research, Basel, Switzerland

5 Institute of Pharmaceutical Sciences, Department of Chemistry and Applied Biosciences, ETH Zürich, Zürich, Switzerland

*Corresponding author. Tel: +41 44 633 39 40; E-mail: allain@mol.biol.ethz.ch

orientation of the miRNA duplex and its interaction with the PAZ and MID domains of Ago. Several factors seem to play a role therein, such as the recognition of the nucleobase at the 5' end of the guide strand by the MID domain of Ago (favoring a U or an A) (Frank *et al*, 2010; Suzuki *et al*, 2015) or the differential thermodynamic stability of the ends of the miRNA duplex (Khvorova *et al*, 2003; Schwarz *et al*, 2003). In flies, the heterodimer Dicer-2/R2D2 senses siRNA asymmetry and participates in RISC loading (Tomari *et al*, 2004). It has been reported, however, that Dcr2/R2D2 involvement in that process is not absolutely required (Nishida *et al*, 2013). In humans, Dicer has been shown to be dispensable for RISC loading (Betancur & Tomari, 2012) while TRBP alone could recognize siRNA asymmetrically (Gredell *et al*, 2010). Other reports suggest that strand selection is rather the result of a subtle interplay of the asymmetry rule, the identity of the 5' nucleotides of the miRNA duplex, and the involvement of Dicer, TRBP, and Ago as multiple sensors (Noland *et al*, 2011; Noland & Doudna, 2013). In the same vein, several reports suggest that TRBP affects the processing of a particular set of pre-miRNAs by shifting the cleavage site of Dicer by one nucleotide, causing the inversion of the guide/passenger strands for a subset of these pre-miRNAs (Fukunaga *et al*, 2012; Lee & Doudna, 2012; Kim *et al*, 2014; Wilson *et al*, 2015).

TRBP was first identified as a protein facilitating HIV infection (Gatignol *et al*, 1991). It is an RNA-binding protein of 39 kDa, which associates with Dicer (Haase *et al*, 2005), influences the precision of pre-miRNA cleavage (Kim *et al*, 2014; Wilson *et al*, 2015), and helps recruiting Ago (Chendrimada *et al*, 2005). TRBP homologs include Loquacious and R2D2 in *Drosophila melanogaster*, RDE-4 in *Caenorhabditis elegans*, DRB1-3,5 in *Arabidopsis thaliana*, Xlrpba in *Xenopus laevis* (Eckmann & Jantsch, 1997), and the PKR activator (PACT) protein in mammals (Peters *et al*, 2001). TRBP and its homologs share the same domain architecture, with three consecutive dsRNA binding domains (dsRBDs) (St Johnston *et al*, 1992; Masliah *et al*, 2013) separated by linkers of various lengths. The affinity of TRBP for dsRNA is essentially conferred by the two N-terminal dsRBDs (Yamashita *et al*, 2011; Takahashi *et al*, 2013), whereas the third dsRBD does not bind dsRNA but interacts with Dicer (Daniels & Gatignol, 2012; Wilson *et al*, 2015). The tertiary structures of the first (dsRBD1) and second (dsRBD2) domains in their free form (Yamashita *et al*, 2011), of dsRBD2 in complex with RNA (Yang *et al*, 2010), and of the third dsRBD (dsRBD3) in complex with a Dicer fragment (Wilson *et al*, 2015) have been elucidated.

To gain deeper insight into the function of TRBP in RNAi processing, we solved the structure of its two N-terminal dsRBDs (dsRBD12) in complex with a highly asymmetric siRNA (EL86) using NMR in conjunction with EPR and single-molecule FRET. We observe that EL86 binds dsRBD12 in two different and opposite orientations, in equal proportions, indicating that EL86 asymmetry does not influence TRBP binding significantly. Our structures show that dsRBD12 covers one side of EL86 along its whole length, leaving the other face potentially accessible to other protein factors. We show experimentally that dsRBD12 does not interfere with pre-miRNA cleavage by Dicer, suggesting the possible existence of a ternary complex TRBP-Dicer-pre-miRNA during the cleavage step.

Results

Individual TRBP's dsRBDs bind EL86 in multiple registers

Protein fragments containing human TRBP (UniProtKB Q15633) dsRBD1 or dsRBD2 were titrated with EL86, a potent siRNA of 19 base pairs with characteristic two-nucleotide 3'-overhangs (Stalder *et al*, 2013; Fig 1A). Formation of each dsRBD-RNA complex was followed by NMR spectroscopy and resulted in large chemical shift changes (Fig EV1A). Mapping these chemical shift perturbations onto the crystal structure of a dsRBD2-dsRNA complex (Ryter & Schultz, 1998) or on the dsRBDs' primary structures reveals three clusters corresponding to the three regions composing the canonical RNA binding surface of dsRBDs (helix α 1, loop 2, N-terminal tip of helix α 2) (Fig EV1B). We conclude from these observations that TRBP's individual domains dsRBD1 and dsRBD2 bind EL86 in a canonical fashion, that is, by interacting with two consecutive minor grooves of an A-form RNA helix (Ryter & Schultz, 1998; Masliah *et al*, 2013).

Next, we measured protein-RNA intermolecular NOEs in the dsRBD1-EL86 and dsRBD2-EL86 complexes using 3D ^{13}C -edited filtered NOESY experiments to assess whether the two domains bind EL86 sequence specifically. Interestingly, a large number of intermolecular NOEs involving dsRBD residues located at the RNA binding surface were observed (Appendix Fig S1A and B). Unexpectedly, residues Ala57 (dsRBD1) and Ala187 (dsRBD2) (all sequence numbers correspond to TRBP wild-type numbering, Fig EV1C), which are located at equivalent positions in the β 1- β 2 loop of each domain, have intermolecular NOEs with at least eight consecutive residues located at the 3' end of each EL86 strand (Fig 1B). In case of single-register binding, Ala57 and Ala187 are expected to have a maximum of two intermolecular NOEs, that is, with two consecutive nucleotides. Therefore, we conclude from this multiplicity of NOEs that TRBP's individual domains do not bind EL86 sequence specifically but rather in multiple registers, unlike the dsRBDs of ADAR2 or NF90, which have been shown to bind dsRNA in single registers (Steffl *et al*, 2010; Jayachandran *et al*, 2016).

Tertiary structures of individual dsRBD1 and dsRBD2

Tertiary structures of TRBP's single domains dsRBD1 and dsRBD2 in the RNA-bound state were determined by NMR spectroscopy. Ensembles of 20 structures with precisions of $0.35 \pm 0.11 \text{ \AA}$ and $0.22 \pm 0.05 \text{ \AA}$ were obtained for dsRBD1 and dsRBD2, respectively (Appendix Table S1). As expected, both domains adopt the canonical dsRBD fold characterized by an $\alpha\beta\beta\beta\alpha$ topology. Interestingly, dsRBD1 presents a short additional α -helix at its N-terminus (referred as helix α 0 hereafter), which folds back on the cleft between helices α 1 and α 2 (Fig 1C). Our structure shows that helix α 0 is stabilized by several hydrophobic interactions involving side-chains from helix α 0 (Ile19, Met22, and Leu23), helix α 1 (Leu34 and Tyr38), and helix α 2 (Leu92, Leu95, and Lys96). A similar extension was reported for the third dsRBD of ADAR 1 where it plays a role in cellular localization (Barraud *et al*, 2014).

Aside from helix α 0, the structures of dsRBD1 and dsRBD2 are very similar, with a backbone r.m.s.d. of $1.22 \pm 0.07 \text{ \AA}$. In addition, our NMR structures superimpose very well with the crystal structures of dsRBD1 in the free state (Yamashita *et al*, 2011) and

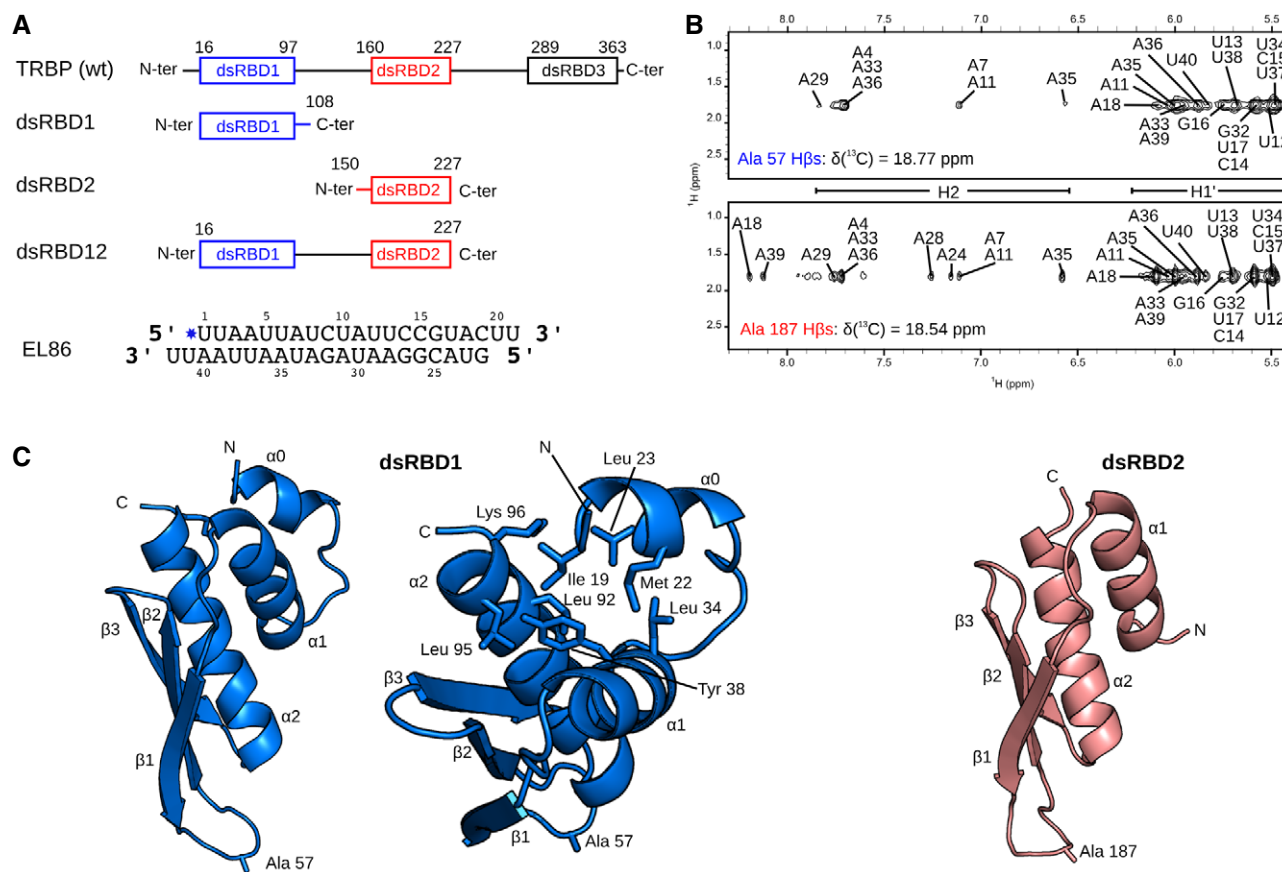


Figure 1. TRBP domains organization, inter molecular NOEs and three dimensional structures of dsRBD1 and dsRBD2.

A (Top) Domain architecture of full-length TRBP. Domain boundaries are indicated above each domain. (Middle) The following TRBP fragments were used in this study: dsRBD1 and dsRBD2, which contain a single dsRBD, dsRBD12, which contains both dsRBD1 and dsRBD2 separated by the native inter-domain linker. (Bottom) Nucleotide sequence and secondary structure of the siRNA EL86.

B Intermolecular NOEs between EL86 H1' protons and Ala57 (dsRBD1, upper) or Ala187 (dsRBD2, lower).

C Solution structures of the EL86-bound forms of dsRBD1 and dsRBD2 determined by NMR spectroscopy. dsRBD1 and dsRBD2 are colored in blue and red, respectively. The N-terminal α -helix extension found in dsRBD1 is denoted as α_0 . Residues Ala57 and Ala187 whose intermolecular NOEs are shown in (B), and residues interacting with helix α_0 protons are represented as sticks.

dsRBD2 bound to dsRNA (Yang *et al*, 2010), yielding backbone r.m.s.d. of 0.82 ± 0.04 Å and 0.85 ± 0.05 Å, respectively. We then compared the NMR fingerprints of dsRBD1, dsRBD2, and dsRBD12 in the presence of EL86 (Fig EV2). We do not observe any significant shift in peak positions and conclude therefore that the structures of dsRBD1 and dsRBD2 do not change significantly when they are expressed in tandem as within dsRBD12, as previously reported (Benoit *et al*, 2013; Wilson *et al*, 2015).

In the dsRBD12-EL86 complex, dsRBD2 binds in two symmetric orientations

Next, we studied siRNA binding by the N-terminal half of TRBP, which contains dsRBD1 and dsRBD2 in tandem (Fig 1A). Intermolecular NOEs collected on the dsRBD12-EL86 complex reveal that both dsRBDs interact with EL86, using the same binding surface as the isolated domains (Appendix Fig S1A–C). Furthermore, the absence of intermolecular NOEs from the inter-domain linker indicates that the linker does not interact with EL86, in agreement

with a study showing that TRBP's linker does not interact with pri-miR-155 (Benoit *et al*, 2013).

Within the dsRBD12-EL86 complex, the only protein side chain having unambiguous intermolecular NOEs is Leu175, which is located in the dsRBD2's loop connecting helix α_1 to strand β_1 (Figs 1C and 2B). Interestingly, the Leu175 methyl group H δ_1 has only four intermolecular NOEs with EL86 ribose H1', whereas at least 10 peaks were observed in the dsRBD2-EL86 complex (Fig 2A). This suggests that dsRBD2 binds in fewer registers in the dsRBD12-EL86 complex than in the dsRBD2-EL86 complex. These four intermolecular NOE peaks could be unambiguously assigned to EL86 residues U2, A3, U23, and A24 (Fig 2A). U2-A3 and U23-A24 sit on opposite EL86 ends, separated by ~ 50 Å. They are thus too far away to be simultaneously contacted by dsRBD2. We conclude therefore that dsRBD2 binds EL86 predominantly in two different registers, in which Leu175 is positioned either at U2-A3 or U23-A24 (Fig 2B).

To validate this interpretation, we measured five pairwise distance distributions between dsRBD2 and EL86 in the dsRBD12-EL86

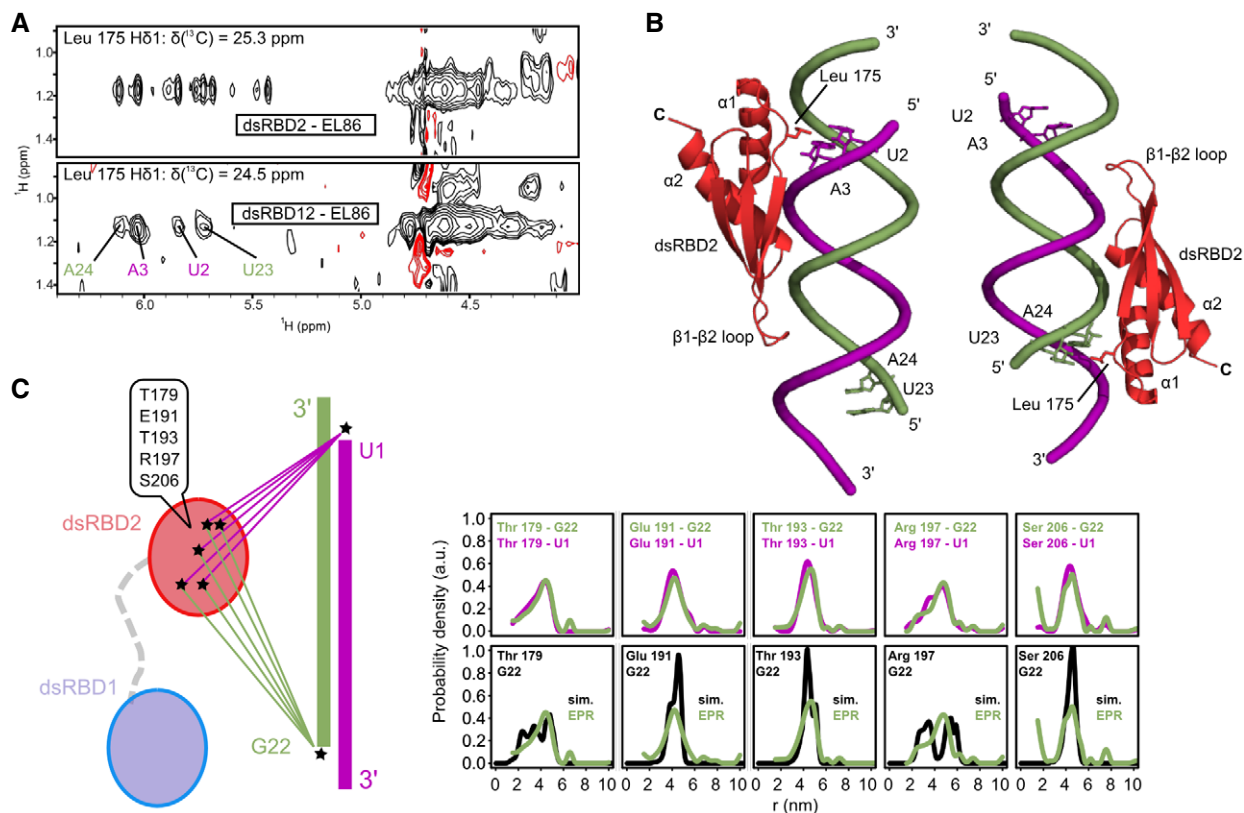


Figure 2. DsRBD2 positioning on EL86 in RNA-bound dsRBD12.

A Selected regions of 3D ^{13}C -edited filtered NOESY spectra collected on the dsRBD2-EL86 (top) and dsRBD12-EL86 (bottom) complexes, showing intermolecular NOE cross-peaks between dsRBD2 Leu175 H δ 1s and EL86 ribose protons. Unambiguous assignments of EL86 H1' are colored in blue (upper strand) and green (lower strand).
B Structural models of the dsRBD2-EL86 complex showing the two orientations compatible with the intermolecular NOEs observed in the dsRBD12-EL86 complex.
C dsRBD2-EL86 distances measured by EPR in the dsRBD12-EL86 complex. (Left, scheme) Five pairwise distance distributions were measured between the dsRBD2 β -sheet surface (Cys179, Cys191, Cys193, Cys197, or Cys206) and the 5' termini (Ura1 or Gua22) of EL86. DsRBD1 (light blue) and dsRBD2 (red) are connected by the native flexible linker (gray dashes). Nitroxide spin labels are represented by asterisks. (Right, upper row) Superposition of experimental distance distributions between dsRBD2 and either EL86 Ura1 (magenta) or Gua22 (green) strands. (Right lower row) Superposition of back-calculated (black) and experimental (green) distance distributions between EL86 Gua22 and each of the five spin labels attachment sites on dsRBD2. Simulated distance distributions were calculated from the two models of dsRBD2-EL86 shown in (B).

complex, using EPR spectroscopy and site-directed spin labeling (SDSL) (Jeschke *et al*, 2006; Bordignon, 2012; López *et al*, 2012). Single nitroxide spin labels were introduced at five specific sites on the dsRBD2 β -sheet surface of single mutants (T179C, E191C, T193C, R197C, S206C), and at either 5' end of EL86, yielding a total of 10 different distances (Fig 2C). All measured distances are between 20 and 50 Å, a distance range that would be expected for dsRBD2 bound to EL86, as the latter is roughly 70 Å in length. We observe virtually identical distance distributions, independent of whether EL86 is labeled on U1 or G22 (Fig 2C). This indicates that the dsRBD2 registers are characterized by identical locations relative to either of the two EL86 termini, which is in agreement with the pattern of intermolecular NOEs observed with Leu175 (Fig 2A and B).

Next, we modeled two canonical dsRBD2-EL86 complexes in which Leu175 was positioned between either U2-A3 or U23-A24 (Fig 2B). dsRBD2-EL86 pairwise distances were simulated using both models and compared with distance distributions determined by EPR (Fig 2C). Very good agreement is observed for the shapes and the means of E191C, T193C and S206C distributions (Fig 2C). Interestingly, the experimental distributions obtained

with T179C and R197C are significantly broader, with significant contributions from both short (2–3 nm) and long (3.5–5.5 nm) distances. As shown by the simulations, each contribution originates from a specific orientation of dsRBD2 on EL86, supporting further the presence of two binding sites revealed by intermolecular NOEs.

DsRBD12 and EL86 form two symmetric, equally populated, complexes

Because of the high level of ambiguity of dsRBD1's intermolecular NOEs, dsRBD1 was positioned with respect to dsRBD2 with the help of residual dipolar couplings (RDCs). Forty-four peptide backbone $\{^{15}\text{N}, ^1\text{H}\}$ RDCs were collected on the dsRBD12-EL86 complex. Calculation of a Pearson's correlation factor (R_p) for dsRBD1 and dsRBD2 yielded values of 0.93 and 0.95, respectively, demonstrating that the RDC dataset is in good agreement with the NMR structures of the individual domains. Interestingly, the two domains have the same alignment tensors, with magnitudes of 10.3 ± 0.5 Hz and 10.8 ± 0.4 Hz, and rhombicities of 0.25 ± 0.05 and 0.29 ± 0.05 for

dsRBD1 and dsRBD2, respectively (Appendix Table S2). This indicates that the relative orientation of dsRBD1 with respect to dsRBD2 is well defined and can be determined by analyzing the set of RDCs within a single coordinate frame common to both domains.

Fourteen models of the dsRBD12-EL86 complex were built, in which dsRBD2 was fixed at one of the two positions determined previously, whereas dsRBD1 was positioned in any remaining accessible register. The agreement of each model with the full RDC dataset was evaluated using a single alignment tensor for both dsRBDs. The correlation factors R_p and the r.m.s.d. values calculated for the different models vary significantly, with values from 0.71 to 0.93 and 4.1 to 8.0 Hz, respectively, indicating that our RDC dataset is a sensitive probe of the relative orientation of the two domains (Fig 3A). For each of the two dsRBD2 positions, two dsRBD1 registers yielded minimal r.m.s.d. and maximal R_p values, and hence were compatible with the RDCs. These registers (#3 and #5, Fig 3A and B, green and magenta) are characterized by anti-parallel and parallel arrangements of the two domains, respectively.

To resolve this ambiguity, six inter-domain distance distributions were measured using EPR spectroscopy with SDSL (Jeschke *et al*, 2006; Bordignon, 2012; López *et al*, 2012) and compared with the corresponding distance distributions calculated in the models compatible with the RDCs. As shown by overlaying the experimental and simulated distance distributions, the configurations with the two domains pointing in opposite directions are in good agreement with the EPR data, whereas the configurations featuring parallel domains deviate significantly, especially for the distances Cys63-Cys191, Cys63-Cys197, and Cys65-Cys193 (Fig 3C). Therefore, we conclude that in solution, the relative orientation of dsRBD1 and dsRBD2 is well defined in the dsRBD12-EL86 complex, with the two domains predominantly pointing in opposite directions (anti-parallel orientation). Along with our finding that dsRBD2 has two main binding sites in the dsRBD12-EL86 complex, we come to the conclusion that dsRBD12-EL86 complex formation yields two major species (referred to as complexes “A” and “B” hereafter), in which dsRBD1-dsRBD2 relative orientation is identical.

We then used single-molecule FRET to quantify the relative occurrence of complexes A and B. With single-molecule FRET, the distance-dependent energy transfer between a donor and an acceptor fluorophore is probed, both of which are conjugated to the molecules of interest (Ha & Selvin, 2008). Because single molecules rather than ensemble averages are measured, the method provides an additional possibility to resolve structural heterogeneity and obtain information about the relative occurrence of the underlying configurations. To ensure that the fluorophores do not affect the function of the protein, we first quantified the affinity of labeled dsRBD12 toward EL86 (Fig EV3A and B). Our results ($K_D = 210 \pm 30$ pM) are in agreement with the affinity of unlabeled dsRBD12 for a 21 bp duplex ($K_D = 250$ pM) previously quantified by isothermal titration calorimetry (Yamashita *et al*, 2011), indicating that the dyes have a negligible influence on TRBP’s function. To investigate the conformations of dsRBD12 in complex with EL86, EL86 was labeled at its 3’-end with the FRET donor Cy3B. The FRET acceptor CF660R was site specifically incorporated into dsRBD12 via a Cys residue introduced at position 100 (dsRBD12 M100C/C158S) or using the naturally occurring Cys residue at position 158 (dsRBD12 M100S), respectively. For both dsRBD12 variants, the two different domain arrangements are expected to lead to

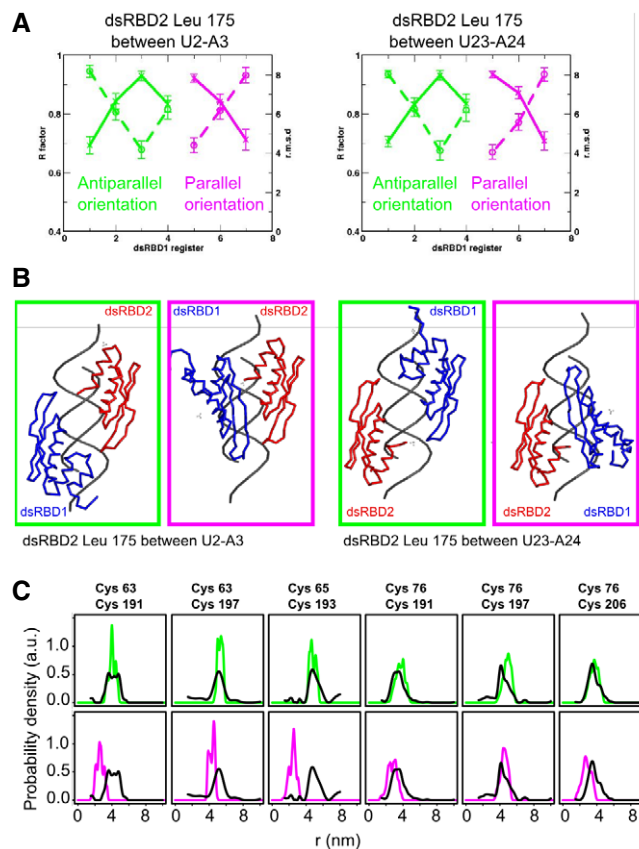


Figure 3. DsRBD1 positioning relative to dsRBD2 in RNA-bound dsRBD12.

- A** RDCs fitting as a function of dsRBD1-dsRBD2 relative orientation. Fourteen models of the dsRBD12-EL86 complex were built (not shown), in which dsRBD2 was fixed in two registers by “anchoring” Leu175 between either Ura2-Ade3 (left) or Ura23-Ade24 (right), and the position of dsRBD1 on EL86 was systematically shifted. R.m.s.d. values (dashed lines) and Pearson’s correlation coefficients (solid lines) are depicted for each model. RDC fitting with models where dsRBD1 and dsRBD2 point in opposite or in the same directions are shown in green and magenta, respectively.
- B** Each position of dsRBD2 (red) yields two possible binding registers for dsRBD1 (blue), due to the intrinsic degeneracy of RDCs. Solutions in which the two domains are “parallel” or “anti-parallel” are represented in magenta and green frames, respectively.
- C** Comparison of EPR (black) and simulated (green or magenta) dsRBD1-dsRBD2 pair-wise distances. Inter-domain distances were simulated using either the anti-parallel (upper row, green curves) or the parallel (lower row, blue curves) models of dsRBD12-EL86 shown in (B).

pronounced differences in transfer efficiency because of different inter-dye distances (Fig 4A).

Indeed, as shown in Fig 4B (top), two peaks are observed in the resulting transfer efficiency histograms. For dsRBD12 M100C/C158S, the peak centered at a transfer efficiency of 0.4 corresponds to complex A, and the peak at 0.9 to complex B. In the case of dsRBD12 M100S, the inter-dye distances of the two configurations are more similar, resulting in a more pronounced overlap of the two transfer efficiency peaks at 0.6 (complex B) and 0.9 (complex A), respectively, consistent with the intermolecular distances expected from the structural models (Fig 4B). The relative populations of the two configurations were quantified by peak integration. To obtain accurate positions and shapes of transfer efficiency distributions for

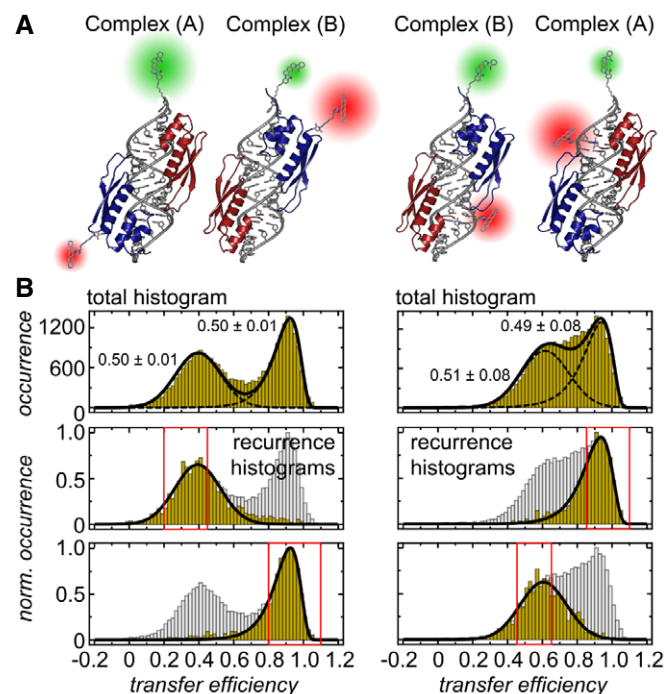


Figure 4. Quantifying the relative occurrence of the two possible configurations of dsRBD12 on EL86 by single-molecule FRET.

- A** Cartoons of CF660R-labeled dsRBD12 C158S (left) and dsRBD12 M100S (right) bound to Cy3B-labeled EL86. The different domain arrangements of dsRBD12 on EL86 are characterized by different inter-dye distances, which were approximated as distances between their attachment points (as M100 is not resolved in the solution structure, the nearest resolved neighbor G98 was used, resulting in an uncertainty of 7 Å, i.e., the contour length of two residues).
- B** Transfer efficiency histograms of CF660R-labeled dsRBD12₂₂₋₂₃₅ C158S (left) and dsRBD12₂₂₋₂₃₅ M100S (right) in complex with Cy3B-labeled EL86. Top: Transfer efficiency histograms exhibit two subpopulations that are equally likely to occur. Errors associated with relative occurrences correspond to the standard deviation. Bottom: Recurrence transfer efficiency histograms were used to extract subpopulation-specific fit parameters. Red boxes highlight the initial transfer efficiency range ΔE . The recurrence interval T was set to (0, 10 ms). See Materials and Methods for details.

the fit, we performed recurrence analysis (Hoffmann *et al.*, 2011), followed by fitting subpopulation-specific recurrence histograms to empirical fit functions (Fig 4B, bottom). The resulting peak parameters were then used to fit the complete histograms (Figure 4B, top). Based on the peak integrals, we observed very similar populations for complexes (A) and (B), both for dsRBD12 M100C/C158S (0.50 ± 0.01) and dsRBD12 M100S, although the overlap of the peaks resulted in greater uncertainty for the latter (complex (A): 0.49 ± 0.08 ; complex (B): 0.51 ± 0.08). Very similar results were obtained with a highly asymmetric siRNA (pp-luc, Fig EV3C), and a symmetric siRNA (sod1, Fig EV3D), demonstrating that the orientation of the two dsRBDs and the relative population of the two complex forms is independent of the sequence.

In summary, single-molecule FRET demonstrates (i) that dsRBD12 binding to EL86 results in two major configurations and (ii) that the relative occurrence of these two conformers is very similar. This indicates that the interactions in the two binding modes are

isoenergetic, and the dsRBD12-RNA interactions are thus unlikely to be sequence-specific.

dsRBD12 binding surface on EL86 resembles a half-cylinder

Using the structural insight gained from NMR and EPR experiments, several ambiguities in intermolecular NOEs assignment could be resolved, providing supplementary distance restraints for structure calculations. The intense intermolecular NOEs from the methyl groups of Ala57 and Ala187, located at equivalent positions in the $\beta 1$ - $\beta 2$ loops of dsRBD1 and dsRBD2, were assigned to five EL86 resonances: C14 (H1'), C15 (H1'), A35 (H1'), A36 (H1'), and A36 (H2) (Fig 5A). The weaker intermolecular NOEs from Thr30, Thr40 (dsRBD1), Val161, and Val169 (dsRBD2) to EL86 H1' protons could also be assigned (Fig 5A). Remarkably, Thr40 and Val169, both of which are located at the C-terminus of dsRBD1 and dsRBD2 $\alpha 1$ helices, have identical NOE patterns (C19 H1' and A40 H1'), further supporting the identical registers of dsRBD1 and dsRBD2 in both complexes. Two sets of distances were derived from these intermolecular NOEs and were used as structural restraints to calculate two structures of the dsRBD12-EL86 complex: In complex A, the dsRBD1 (dsRBD2) $\beta 1$ - $\beta 2$ loop region was constrained to lie between A35 and A36 (C14 and C15), whereas in complex B, the constraints were inverted, with dsRBD1 (dsRBD2) $\beta 1$ - $\beta 2$ loop region constrained between C14-C15 (A35-A36). Calculations yielded two well-defined ensembles (Appendix Table S3 and Fig 5B) in which dsRBD1 and dsRBD2 point in opposite directions along the axis of EL86 helix: The $\alpha 1$ helices are located at the extremities of EL86, whereas the $\beta 1$ - $\beta 2$ loops are located near the center in a head-to-head fashion (Fig 5B). The good precision of the structure ensembles (backbone r.m.s.d. of 0.87 ± 0.18 Å and 0.83 ± 0.15 Å for complexes A and B, respectively, Appendix Table S3) allows for a detailed analysis of the structures.

In the two complexes, dsRBD1 and dsRBD2 bind EL86 via the dsRBD canonical binding surface. The two domains point in opposite directions and the two complexes are very similar, albeit dsRBD1 and dsRBD2 are swapped (Fig 5B). Remarkably, the two domains bind one side of the RNA helix (a half-cylinder) over the whole length of EL86. The remainder of the RNA surface, which is solvent-exposed in our structures, corresponds to the other half-cylinder of the EL86 RNA helix (Fig 5C). The phosphate backbone of EL86 is recognized by the evolutionarily conserved KKxAK motif, corresponding to Lys80, Lys81, Lys84 and Lys210, Lys211, Lys214 in dsRBD1 and dsRBD2, respectively (Fig EV4). The $\beta 1$ - $\beta 2$ loop of dsRBD2 is well defined and interacts with the minor groove of EL86. In particular, the Ala187 methyl group makes hydrophobic contacts with A35 and A36, and C14 and C15 in complexes A and B, respectively (Fig EV4). In complex A, the carbonyl group of Ala187 is hydrogen bonded to the amino group of G27. In complex A (B), His188 N δ 1 makes a hydrogen bond to the 2'-OH of C15 (A36), whereas the peptide carbonyl group interacts with the 2'-OH of G27 (U6), bridging the two RNA strands across the minor groove, as reported previously for the second dsRBD of *X. laevis* RNA-binding protein (Ryter & Schultz, 1998). The $\beta 1$ - $\beta 2$ loop of dsRBD1 is less well defined, but Ala57 and His58 make essentially the same interactions as Ala187 and His188 (Fig EV4). Residues Ile32, Ser33, Gln36, Glu37, Thr40, and Arg41 located within dsRBD1 helix $\alpha 1$ and residues Val161, Gln165, Glu167, Val169, Gln170 located within

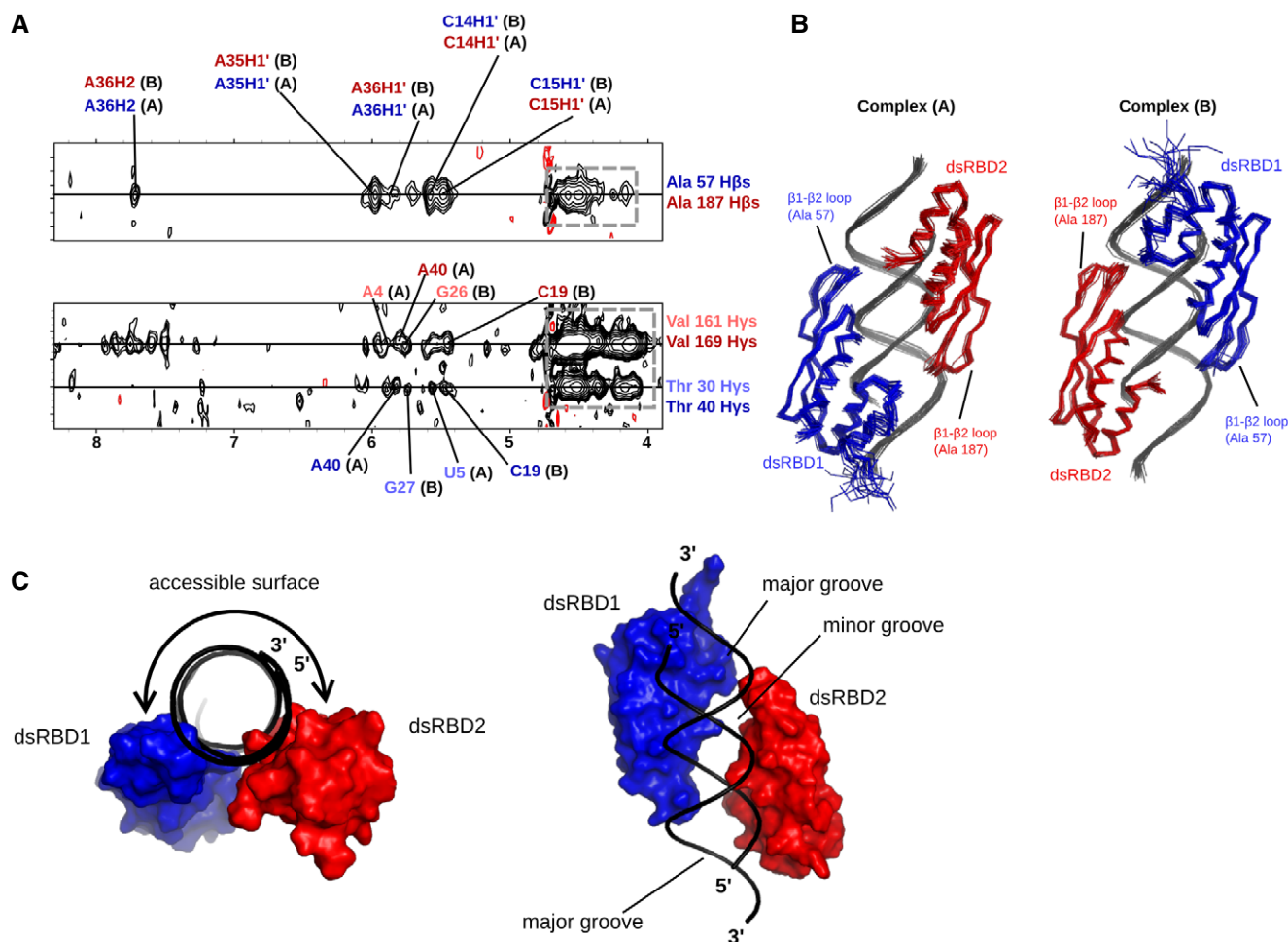


Figure 5. Three dimensional structures of the dsRBD12-EL86 complex.

- A** Selected regions of the ^{13}C -edited filtered NOESY spectrum recorded on the dsRBD12-EL86, showing intermolecular NOEs between Ala57 Hβs (dsRBD1)/Ala187 Hβs (dsRBD2) and EL86 H1' protons. Blue (red) assignment labels correspond to dsRBD1-Ala57 (dsRBD2-Ala187). The particular domain arrangement corresponding to each assignment is designated by A or B, respectively. NOE peaks in the gray dashed box correspond to EL86 H4'/H5'/H5'' protons and carry very limited, if any, sequence-related information.
- B** Structure ensembles of complexes A and B calculated using experimental intermolecular distance restraints and residual dipolar couplings. dsRBD1 and dsRBD2 are colored in blue and red, respectively.
- C** Global view of the dsRBD12-EL86 complex showing the half-cylinder RNA region left solvent-exposed, and potentially accessible to other proteins. dsRBD1 and dsRBD2 surfaces are represented in blue and red, respectively. EL86 is represented as a black cartoon.

dsRBD2 helix $\alpha 1$ make numerous hydrophobic and polar contacts in the RNA minor groove with ribose moieties (Fig EV4). In addition, two side-chains (Lys29 and Thr30) located in the loop connecting dsRBD1 helices $\alpha 0$ and $\alpha 1$ interact with ribose sugars on each side of the RNA minor groove.

We then used EL86 variants, in which a 2'-O-methoxyethyl group was incorporated at each single position on the guide strand (upper strand in Fig 1A) during chemical synthesis, to knock down a cognate mRNA in HeLa cells. As observed in other studies (Prakash *et al*, 2005; Jackson *et al*, 2006), the knockdown efficiency was affected in a position-dependent manner (Fig EV5). The strongest effects are observed when either position 1, 2, or 14 is modified. Based on our structures, U1 does not interact with dsRBD12, and C14 is contacted by the methyl group of Ala57 (dsRBD1) or Ala187 (dsRBD2), in complexes B and A,

respectively. Furthermore, U2 forms contacts with dsRBD2 Leu175 in complex A (Fig EV5). Consequently, one could speculate that the reduced efficiency might originate from a weakened interaction with TRBP.

We propose that the spatial arrangement of TRBP dsRBDs on EL86 primarily results from the recognition of the structural features of the A-form RNA helix. We note that this particular configuration of the two domains is the only way to position helix $\alpha 1$ at the RNA ends for both domains simultaneously. This is reminiscent of a trend observed in other dsRBD-dsRNA structures, where helix $\alpha 1$ often interacts with stem-loop junctions (widened minor groove), whereas the $\beta 1$ - $\beta 2$ loop is found in more regular RNA stems (Steffl *et al*, 2010; Wang *et al*, 2011). Finally, it is noteworthy that dsRBD12 covers a continuous RNA region of 19 base pairs resembling a half-cylinder, while the second half of the RNA surface

remains solvent-exposed. It is therefore tempting to speculate that Dicer binds on this surface during pre-miRNA processing.

DsRBD12 binds shEL86 during Dicer processing under single-turnover conditions

We designed a pre-miRNA (shEL86) by extending EL86 by two additional base pairs and a nine-residue terminal loop (Fig 6A; Bofill-De Ros & Gu, 2016). shEL86 was 32 P-radiolabeled at its 5'-end and used as a substrate for Dicer under single-turnover conditions. Denaturing PAGE analysis reveals two cleavage products that are 22 nt and 21 nt in length, respectively (Fig 6B). These two bands result from the Dicer cleavage of shEL86's 5' arm at two consecutive positions and display an intensity ratio of 2:1 (Fig 6A). Next, we formed TRBP dsRBD12-shEL86 complexes by incubating 12 nM shEL86 with dsRBD12 at increasing concentrations (5–400 nM), followed by Dicer-mediated cleavage. The dsRBD12-EL86 complex displays a dissociation constant of 0.21 nM (Fig EV3B), and hence, dsRBD12 and shEL86 molecules are mostly associated within complexes under our experimental conditions. At a dsRBD12:shEL86 ratios below 10:1, we do not observe any statistically significant difference in the amount of RNA cleavage products despite a slight cleavage increase in the presence of TRBP up to 1:1 (Fig 6B, lanes 2–6). In contrast, we observe a clear inhibition of product formation at dsRBD12:EL86 ratios greater than 10:1 (Fig 6B, lanes 7–10). We therefore conclude that TRBP dsRBD12 does not interfere with Dicer cleavage of shEL86 unless present in large excess, where two dsRBD12 molecules are likely to bind simultaneously. These results are in agreement with our structure-based proposal that dsRBD12 and Dicer both bind shEL86 at two distinct and non-overlapping regions during shEL86 cleavage at its terminal loop.

Modeling of a dsRBD12-EL86-Dicer ternary complex

We then built a structural model of a ternary TRBP-RNA-Dicer complex to understand better how TRBP and Dicer may act during pre-miRNA processing. For this purpose, we docked the X-ray structure of the PAZ-platform-Connector-RNA complex (Tian *et al*, 2014) onto our dsRBD12-EL86 structure by superposing the RNA present in both structures. We then positioned EL86 onto Dicer's RNase III catalytic center in the following way: First, we docked the X-ray structure of the Aa RNase III-RNA complex (Gan *et al*, 2006) onto the PAZ-dsRBD12-EL86 assembly by superimposing the two RNA strands present in the RNase III structure onto the EL86 end distal from the PAZ domain. Second, we overlaid the X-ray structure of Dicer RNase III (Du *et al*, 2008) onto the Aa RNase III structure using well-conserved regions. As a result, we obtained a preliminary model in which TRBP dsRBD12, Dicer's RNase III, PAZ, and platform domains are all docked on the surface of EL86. Remarkably, each domain is found to interact with a distinct EL86 region, and the ternary complex is devoid of steric clashes. Moreover, the model suggests a possible interaction between the C-terminal dsRBD of Dicer with both TRBP dsRBD2 and the RNA minor groove (Fig 7A). In this context, the dsRBD of Dicer does not compete for EL86 with the dsRBDs of TRBP. We then fitted our model into the EM envelope of apo-Dicer (Taylor *et al*, 2013). Here, we could also position the X-ray structures of the first and third domains of RIG-I (Kowalinski *et al* 2011) and of the TRBP-dsRBD3-Dicer-PBD complex (Wilson *et al*, 2015) into the EM density corresponding to the base branch (Lau *et al* 2012). The volume of the Dicer map could accommodate the entire structural model, with the

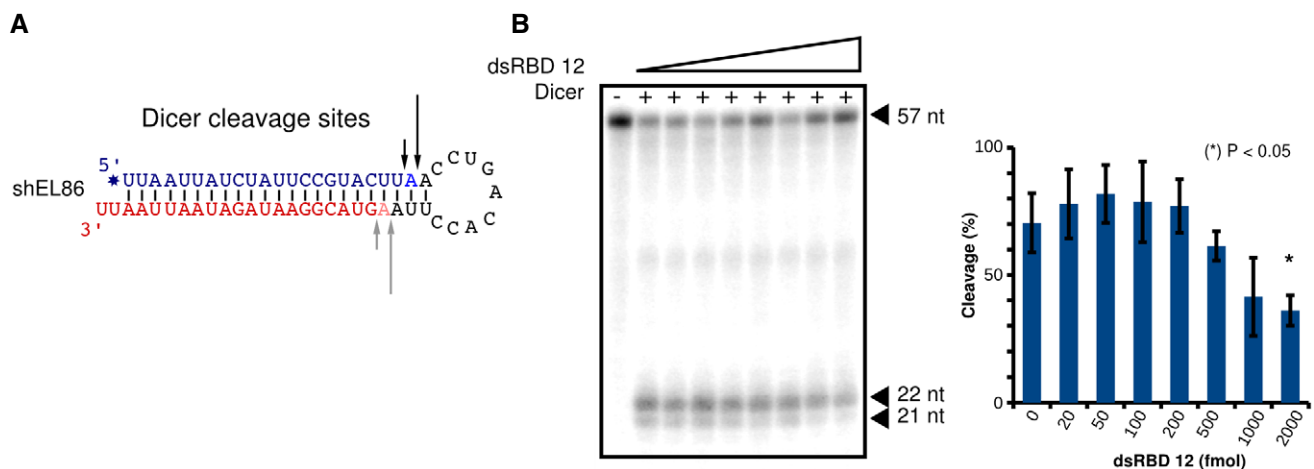


Figure 6. Dicing assay: shEL86 cleavage by Dicer.

- A** Secondary structure of shEL86. The 5' and 3' arms are colored blue and red, respectively. The 32 P-radiolabel incorporated at the 5' end is indicated by a blue asterisk. Dicer's cleavage sites experimentally determined are indicated by black arrows. Gray arrows indicate Dicer's cleavage sites inferred from the cleavage sites positions on the 5'-arm.
- B** (Left) Representative denaturing polyacrylamide gel showing uncleaved RNA substrate (57 nucleotides) and two cleavage products of 21 and 22 nucleotides. Lane 1: negative control in the absence of Dicer; lanes 2–9: Dicer cleavage in the presence of increasing concentration of dsRBD12 (0, 20, 50, 100, 500, 200, 1,000, 2,000 fmol). (Right) Quantification of shEL86 cleavage for increasing dsRBD12 concentrations, calculated as $100 \times \text{RNA-product} : \text{total-RNA}$. Each datapoint represents the average \pm SD of three experimental replicates. The cleavage yields in the absence and in the presence of dsRBD12 were compared with a Student's t-test. The asterisk denotes a P -value of < 0.05 .

exception of TRBP dsRBD12, as expected. In particular, the relative orientation of the PAZ-RNase III domains, obtained indirectly by overlaying RNA molecules from different structures, matches the EM density well (Fig 7B). We arbitrarily chose to orient our dsRBD12-EL86 structure on Dicer's RNase III domains such that dsRBD1 and dsRBD2 are located near the PAZ and the helicase domains, respectively. In our model, the distances between the N-terminus of dsRBD3 and the C-terminus of TRBP dsRBD1 and dsRBD2 are 75 and 40 Å, respectively. DsRBD2 and dsRBD3 are connected by a linker of 30 amino acids, which can in theory span up to 108 Å in an extended conformation. Our model is therefore compatible with the length of TRBP dsRBD2-3 inter-domain linker. It does not permit, however, to predict the relative orientation of two N-terminal dsRBDs of TRBP during pre-miRNA processing.

Discussion

Role of TRBP in mi/siRNA asymmetry

Guide strand selection is a crucial process, since it determines which mRNAs are to be translationally repressed in the cytoplasm. Likewise, failure to accurately predict the guide strand when designing a siRNA will result in "off-target" effects (Bofill-De Ros & Gu, 2016). The molecular mechanism governing strand selection is not well understood, albeit it is generally agreed that the fate of the two si/miRNA strands is determined after mi/siRNA duplex loading into Argonaute. The stability of the mi/siRNA duplex termini has been proposed to be one of the determinants of strand selection and is based on the observation that the RNA strand with the less stable 5' end is usually selected as the guide (Khvorova *et al*, 2003; Schwarz *et al*, 2003). The heterodimers R2D2/Dcr-2 and Loqs/Dcr-2 in flies, and Dicer/TRBP in humans, are able to bind asymmetric siRNA duplexes with a well-defined orientation (Tomari *et al*, 2004; Noland *et al*, 2011; Tants *et al*, 2017). It has also been shown that human Dicer is dispensable for asymmetric RISC assembly (Betancur & Tomari, 2012). Consequently, the proteins TRBP (Gredell *et al*, 2010) and its *Drosophila* homolog R2D2 (Tomari *et al*, 2004) were proposed to transduce si/miRNA thermodynamic asymmetry into strand selection. The protein Ago has also been shown to play a role in guide strand selection, and structural studies have unveiled a direct readout of the 5' nucleobase by Ago MID domain (Frank *et al*, 2010; Suzuki *et al*, 2015).

Here, we studied the interaction of TRBP's N-terminal dsRBD12 (Yamashita *et al*, 2011; Benoit *et al*, 2013) with a highly asymmetric siRNA (EL86) exhibiting a strand selection bias of several orders of magnitude (Stalder *et al*, 2013). Our results show that these two molecules form two distinct complexes in solution that are equally populated. Essentially, the two complexes differ by a 180° re-orientation of EL86 with respect to the dsRBD12, or equivalently, by a swapping of dsRBD1 and dsRBD2 binding sites. Very similar results are obtained for the asymmetric siRNA pp-luc, and the symmetric siRNA sod1 (Fig EV3C and D). We therefore propose that TRBP's unbiased binding behavior is not specific to EL86. Rather, it appears to be a general property of the protein. Within our experimental setting, siRNA asymmetry does not influence TRBP binding, which

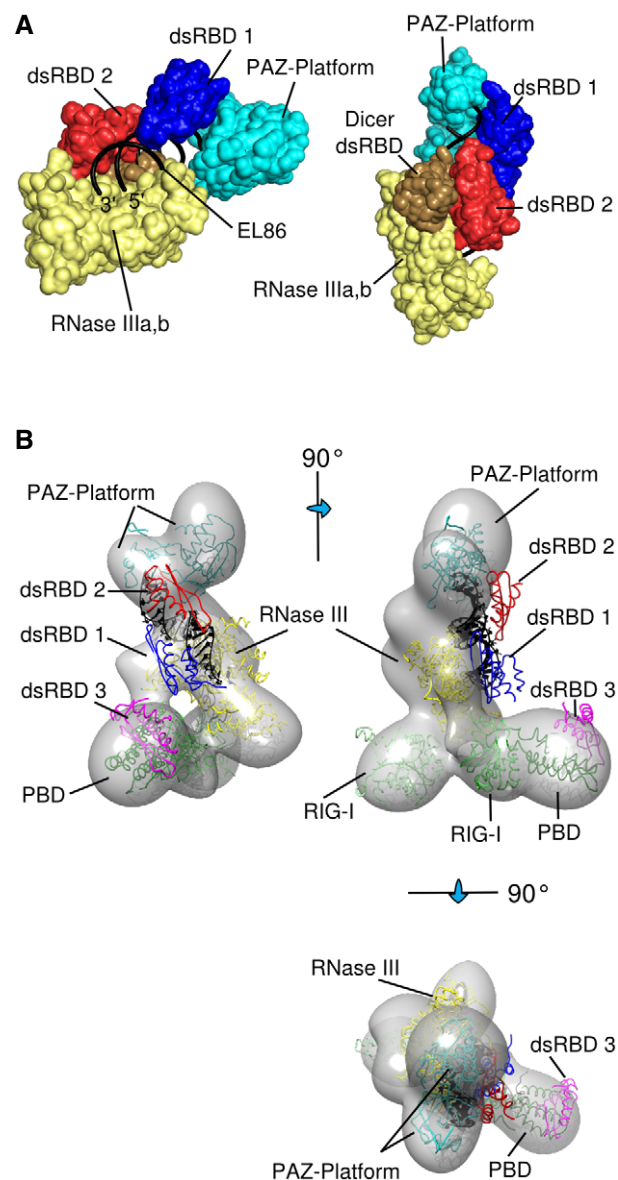


Figure 7. Three dimensional modeling of a putative ternary complex, showing shEL86 cleavage product binding simultaneously to Dicer and TRBP dsRBD12.

A (Left) Spatial arrangement of Dicer's RNase III (yellow, PDB id 3C4B; Du *et al*, 2008) and PAZ-Platform (cyan, PDB id 4NHA; Tian *et al*, 2014) domains resulting from their docking onto EL86 (black). Each domain interacts with a distinct RNA region without any steric clash. (Right) Side-view showing the proximity of Dicer's dsRBD (gold) with TRBP dsRBD2 (red), dsRBD1 (blue), and dsRBD3 (magenta).

B The distance between TRBP dsRBD2 and dsRBD3 was estimated by docking within the EM envelope of apo-Dicer (EMD-5601; Taylor *et al*, 2013) our 3D model for the dsRBD12-EL86-PAZ-Platform-RNase III, RIG-I domains 1,3 (PDB id 4A36; Kowalinski *et al*, 2011) and TRBP-dsRBD3-Dicer-PBD (PDB id 4WYQ; Wilson *et al*, 2015). Orthogonal views are shown.

suggests that TRBP *alone* cannot "sense" siRNA or miRNA asymmetry. It cannot be excluded, however, that TRBP participates to asymmetric si/miRNA loading into Ago. It has been reported in a very recent study that in flies, the heterodimer Loqs-PD-Dcr2 is able to

discriminate the two ends of an asymmetric RNA. This ability relies on a moderate intrinsic binding preference of Loqs-PD for the most stable end of a 21-bp siRNA (Tants *et al*, 2017). This apparent difference in the mode of binding of these functionally homologous proteins with regard to RNA asymmetry sensing is likely to be caused by a sequence divergence between the two proteins, in particular within the residues binding RNA and in the length of the inter-domain linker, which is shorter in Loqs-PD. Additionally, the longer siRNA substrate used in the work by Tants *et al* (two base pairs longer) might also influence the mode of binding.

TRBP's influence on pre-miRNA processing

The processing of pre-miRNA by Dicer, which consists in the excision of the pre-miRNA terminal loop, is regulated, at least partly, by TRBP. *In vitro*, TRBP has been shown to accelerate or inhibit the pre-miRNA cleavage rate (Lee & Doudna, 2012), and to maintain pre-miRNA efficient processing in a RNA-crowded environments (Fareh *et al*, 2016). Furthermore, for several pre-miRNAs, TRBP shifts the position of the Dicer-cleavage site, resulting in miRNAs one nucleotide longer (Fukunaga *et al*, 2012; Lee & Doudna, 2012; Wilson *et al*, 2015). This change of the 5' nucleotide of the miRNA's 3' arm can lead in some particular cases to an inversion of the guide/passenger strands (Kim *et al*, 2014; Wilson *et al*, 2015). The molecular mechanism whereby TRBP produces its effects is not well understood yet. However, the simplest hypothesis is that TRBP interacts with the pre-miRNA and/or Dicer, during pre-miRNA processing. The siRNA used in this study (EL86) has 19 base pairs and 2-nucleotide 3' overhangs at both ends. It is therefore very similar, with regard to its size and secondary structure, to a miRNA product resulting from the processing of a pre-miRNA. Interestingly, our structure of TRBP dsRBD12 in complex with EL86 shows that dsRBD12 interacts with one face of the RNA, covering a surface resembling a half-cylinder (Fig 5). Our dicing assay performed on shEL86, an RNA hairpin derived from EL86 and mimicking a pre-miRNA, carried out in the presence or in the absence of TRBP, shows that TRBP does not compete with Dicer for binding shEL86 (Fig 7). We propose therefore that during pre-miRNA processing, Dicer and TRBP dsRBD12 bind the pre-miRNA simultaneously, on two distinct, non-overlapping, surfaces. Using the structures of various Dicer's fragments in complex with RNA along with our structure of TRBP-dsRBD12 in complex with EL86, we built a structural model of a ternary Dicer-EL86-dsRBD12 complex, which mimics a reaction intermediate resulting from pre-miRNA dicing (Fig 7A). Furthermore, our model suggests that TRBP-dsRBD12 can bind the miRNA region of a pre-miRNA, without causing steric clashes with Dicer. This model provides therefore a physically realistic description of a putative Dicer-miRNA-dsRBD12 complex, which suggests that TRBP's effect on the size of the miRNA product could result from dsRBD12 capacity to affect the structure of the pre-miRNA's stem (e.g., by stabilizing looped-out nucleotides) (Fukunaga *et al*, 2012; Lee & Doudna, 2012; Kim *et al*, 2014; Wilson *et al*, 2015). According to our model, the formation of a stable Dicer-pre-miRNA-dsRBD12 complex competent for pre-miRNA processing necessitates a pre-miRNA with a dsRNA length of 19 base pairs. This is in agreement with a previous report demonstrating that TRBP acts as a gate-keeper, preventing Dicer to engage in stable interactions with non-cognate substrates (Fareh *et al*, 2016).

Materials and Methods

Protein expression and purification

Amino acid numbering of the various TRBP fragments used in this study refers to the wild-type human TRBP (UniProtKB Q15633). In brief, DNA fragments encoding TRBP dsRBD1 (16–108), dsRBD2 (150–227), or dsRBD12 (16–227) were inserted in pet28a vectors, modified to include a tobacco etch virus (TEV) protease cleavage site immediately upstream of the multi-cloning site. Proteins were overexpressed in *Escherichia coli* BL21(DE3) Codon plus (RIL) cells using standard techniques. Hexa-histidine tags were removed by TEV digestion. A detailed purification protocol can be found in Methods section within the Appendix.

NMR spectroscopy and structure calculations

All the NMR experiments were recorded at 313 K. Data were processed using Topspin 3.1 (Bruker) and analyzed with Sparky (T. D. Goddard and D. G. Kneller, SPARKY 3, University of California, San Francisco). Spectra analysis and structure calculation were carried out using standard procedures described elsewhere (Dominguez *et al*, 2011). Further details are provided in the Methods section within the Appendix.

EPR spectroscopy and DEER analysis

The samples for DEER measurements were prepared as solutions of ca. 100 μ M of protein–RNA complex in 1/1 D₂O/D-glycerol (v/v) mixture. For each sample, about 30 μ l of such mixture was placed into a quartz tube of 3 mm outer diameter and frozen by immersion into liquid nitrogen and stored until measurement. Further details concerning instrumentation, data acquisition and data analysis are to be found in Methods section within the Appendix.

RNA preparation

EL86 oligonucleotides used in single-molecule FRET experiments were purchased RP-HPLC-purified from Integrated DNA Technologies BVBA (Leuven, Belgium), where EL86up (5'-UUA AUU AUC UAU UCC GUA CUU-3') was functionalized with a biotin at its 3'-end, while a primary amino modifier was incorporated at the 3'-end of EL86down (5'-GUA CGG AAU AGA UAA UUA AUU-3'). Oligonucleotides used in NMR and EPR experiments were chemically synthesized on an Äkta Oligopilot plus OP100 (GE Healthcare). Further information is provided in the Methods section within the Appendix.

Single-molecule spectroscopy

Single-molecule FRET experiments were conducted at 295 K on freely diffusing molecules with a custom-built confocal microscope equipped with a UplanApo 60 \times /1.20 W objective (Olympus) and a 100- μ m pinhole. Fluorophores were excited alternately using pulsed interleaved excitation (Müller *et al*, 2005) with light of a supercontinuum fiber laser (SC-450-4, Fianium Ltd., Southampton, UK) filtered by a HC543.5/2 band pass for donor excitation and a diode laser emitting at 640 nm (LDH-D-C-640, Picoquant GmbH, Berlin, Germany) for acceptor excitation. Both lasers were operated

at a repetition rate of 20 MHz, and the intensities were adjusted to 50 μ W at the back aperture of the objective. Fluorescence emitted by the sample was collected by the objective and separated according to polarization using a polarizing beam splitter, followed by separation according to wavelength with two dichroic beam splitters (635DCXR, Chroma Technology GmbH, Olching, Germany). Donor detection channels were equipped with ET585/65 m band-pass filters (Chroma Technology GmbH, Olching, Germany) and τ -SPAD avalanche photodiodes (Picoquant, Berlin, Germany). Acceptor detection channels were equipped with LP 647 RU long band-pass filters (Semrock, Inc. Rochester, NY) and SPCM-AQRH-14 avalanche photodiodes (PerkinElmer AG, Schwerzenbach, Switzerland). Photon arrival times were recorded with a HydraHarp 400 time-correlated single-photon counting system (PicoQuant GmbH, Berlin, Germany) at a time resolution of 16 ps. All measurements were conducted in PEGylated sample chambers (Microsurfaces, Inc., Eaglewood, NJ, USA). To study the orientation of dsRBDs on dsRNA, sample solution containing 10 pM Cy3b-labeled RNA (EL86down, sod1down, or pplucdown) and 333 nM unlabeled complement (EL86up, sod1up, or pplucup), 66 pM CF660R-labeled dsRBD12, 15 nM BSA, 0.001% (w/v) Tween-20, dissolved in 20 mM Tris-HCl, 25 mM KCl, pH 7.4 were used. Single-molecule data were recorded for 8–14 h to ensure sufficient statistics for recurrence analysis. To quantify the affinity of dsRBD12 toward dsRNA, sample solutions containing unlabeled EL86, 25 pM Cy3b-CF660R-labeled dsRBD12, 15 nM BSA, 0.001% (w/v) Tween-20, dissolved in 20 mM Tris-HCl, 125 mM KCl, pH 7.4 were measured for 1 h.

Single-molecule data analysis

Photon bursts emitted from fluorescently labeled molecules diffusing through the confocal volume were identified as contiguous intervals of emission with inter-photon times of less than 150 μ s and a minimum number of photons of 30. Subsequently, bursts were corrected for differences in chromophore quantum yields, differences in detection efficiency of the detectors, spectral cross-talk, direct acceptor excitation, and background signal (Schuler, 2007). The stoichiometry ratio, S , of a burst was calculated according to

$$S = \frac{n_{\text{tot,Dex}}}{n_{\text{tot,Dex}} + n_{\text{tot,Aex}}}$$

where $n_{\text{tot,Dex}}$ and $n_{\text{tot,Aex}}$ denote the corrected total number of photons emitted after donor or acceptor excitation, respectively (Müller *et al*, 2005). Bursts with $0.3 < S < 0.65$ were used to calculate the transfer efficiency E as

$$E = \frac{n_A}{n_A + n_D}$$

where n_D and n_A are the corrected donor and acceptor photon counts upon donor excitation within a burst. Transfer efficiencies were binned in histograms.

To obtain subpopulation-specific transfer efficiency histograms for probing the orientation of dsRBDs on dsRNA, we used recurrence analysis of single particles (RASP) (Hoffmann *et al*, 2011). RASP relies on the observation that at sample concentrations in the low picomolar range and for timescales up to several tens of milliseconds, the probability that two consecutive fluorescent bursts

originate from the same molecule is higher than that they stem from different molecules. Provided that conformational dynamics occur on a timescale much slower than the diffusion time, two consecutive bursts are therefore likely to yield the same transfer efficiency. Based on this recurrence behavior, subpopulations were isolated from each measurement using an initial transfer efficiency range ΔE (indicated as red boxes in Figs 4 and EV3C and D) and a recurrence interval between 0 and 10 ms. The resulting recurrence histograms were fitted to Gaussian or lognormal peak functions to determine their positions and shapes. These fit functions were then used to describe the complete histograms (8–14 h measurements), where only the peak amplitudes were allowed to vary. The relative occurrences of subpopulations were calculated from the resulting peak areas. The corresponding standard deviations were estimated by splitting the recorded data into segments of 1 h, followed by determination of subpopulation-specific relative occurrences through constrained fitting using the peak parameters obtained by RASP.

To quantify the affinity of dsRBD12 toward dsRNA, a binding titration was performed. Transfer efficiency histograms of FRET-labeled TRBP (~25 pM) recorded at 0 and 100 nM dsRNA were described with a single Gaussian (unbound) or lognormal peak function (bound), respectively, and the resulting positions and shapes of the fit functions were fixed for a global fit of all transfer efficiency histograms in terms of a two-state model. As a result, the peak amplitudes of the bound and unbound states are the only adjustable parameters in the fit. The fractional occupancy of unbound and bound states was quantified from the relative peak areas, followed by fitting the data to the binding isotherm

$$\theta = \frac{c_{\text{TRBP}} + c_{\text{dsRNA}} + K_D - \sqrt{(c_{\text{TRBP}} + c_{\text{dsRNA}} + K_D)^2 - 4 c_{\text{TRBP}} c_{\text{dsRNA}}}}{2 c_{\text{TRBP}}}$$

where θ is the fraction of TRBP bound to dsRNA, c_{TRBP} and c_{dsRNA} are the total concentrations of TRBP and dsRNA, respectively, and K_D is the dissociation constant.

Dicing assays

Single turnover shEL86 cleavage by Dicer was carried out as previously reported (Ma *et al*, 2012). Recombinant human Dicer variant 1 (NCBI Accession No. NM_177438) was purchased from OriGene Technologies, Inc. 9620 Medical Center Drive, Suite 200 Rockville, MD 20852, Catalog No. TP319214. The nucleotide sequence of shEL86 is 5'-UUAUUAUCUAUUCUGACUUAACCUGACACCUUAA GUACGGAAUAGAUAAUUAUUU-3'. shEL86 was 5'-end labeled using [γ - 32 P] ATP (Hartmann Analytic GmbH) and T4 polynucleotide kinase (New England Biolabs Inc.). Dicing reaction was performed in 5 μ l of reaction mix consisting of 25 mM Tris (pH 7.0), 25 mM NaCl, 2 mM DTT, 1.5 mM MgCl₂, 1% glycerol, 12 nM shEL86, 120 nM Dicer, 0–400 nM dsRBD12. When present, dsRBD12 was incubated for 15 min with shEL86 prior to Dicer addition. After incubating 30 min at 37°C, the reaction was stopped with 5 μ l of loading buffer (10% glycerol, 20 mM TBE, 6 M urea, 0.1% bromophenol blue) followed by heating at 85°C for 10 min. Substrate and cleavage products were resolved by electrophoresis (16% polyacrylamide, urea 7 M). Gel was dried, and RNA substrate and cleavage products were quantified using a Typhoon Trio (GE Healthcare).

Data availability

The structure coordinates of complex A and complex B have been deposited in the Protein Data Bank (<http://www.rcsb.org>) and assigned the identifiers 5N8M and 5N8L, respectively.

Expanded View for this article is available online.

Acknowledgements

This work has been supported by the CTI grant 11329.1 PFLS-LS to FH-TA and NMK as well as a Sinergia grant from the Swiss National Science Foundation CRSII5_170976 to B.S., F.H.-T.A and G.J. F.A. also acknowledges support from the NCCR RNA and Disease from the Swiss National Science Foundation. We thank Prof. Jonathan Hall (ETH Zürich) for the provision of pre-miRNA samples, Daniel Nettels (University of Zürich) for help with single-molecule FRET analysis and instrumentation. B.S. was supported by the Swiss National Science Foundation.

Author contributions

GM, CM, and FH-TA designed NMR experiments; GM and CM conducted NMR experiments. MY, GM, and GJ designed EPR experiments; MY conducted EPR experiments. SLBK and BS designed smFRET experiments; SLBK conducted smFRET experiments. GM, CM, and AH prepared protein samples. JM, JH, and NM-K designed and synthesized RNA oligonucleotides. GM designed and performed dicing assays. FA and JW designed and conducted RNA silencing assays. All authors analyzed data. GM, CM, SLBK, BS, MY, JH, and FH-TA wrote the manuscript. ALM synthesized the shEL86 RNA.

Conflict of interest

The authors declare that they have no conflict of interest.

References

- Barraud P, Banerjee S, Mohamed WI, Jantsch MF, Allain FH-T (2014) A bimodular nuclear localization signal assembled via an extended double-stranded RNA-binding domain acts as an RNA-sensing signal for transportin 1. *Proc Natl Acad Sci USA* 111: E1852–E1861
- Bartel DP (2004) MicroRNAs: genomics, biogenesis, mechanism, and function. *Cell* 116: 281–297
- Benoit MPMH, Imbert L, Palencia A, Pérard J, Ebel C, Boisbouvier J, Plevin M (2013) The RNA-binding region of human TRBP interacts with microRNA precursors through two independent domains. *Nucleic Acids Res* 41: 4241–4252
- Bernstein E, Caudy AA, Hammond SM, Hannon GJ (2001) Role for a bidentate ribonuclease in the initiation step of RNA interference. *Nature* 409: 363–366
- Betancur JG, Tomari Y (2012) Dicer is dispensable for asymmetric RISC loading in mammals. *RNA* 18: 24–30
- Bofill-De Ros X, Gu S (2016) Guidelines for the optimal design of miRNA-based shRNAs. *Methods* 103: 157–166
- Bordignon E (2012) Site-directed spin labeling of membrane proteins. *Top Curr Chem* 321: 121–157
- Carthew RW, Sontheimer EJ (2009) Origins and mechanisms of miRNAs and siRNAs. *Cell* 136: 642–655
- Chendrimada TP, Gregory RI, Kumaraswamy E, Norman J, Cooch N, Nishikura K, Shiekhattar R (2005) TRBP recruits the Dicer complex to Ago2 for microRNA processing and gene silencing. *Nature* 436: 740–744
- Daniels SM, Gatignol A (2012) The multiple functions of TRBP, at the hub of cell responses to viruses, stress, and cancer. *Microbiol Mol Biol Rev* 76: 652–666
- Denli AM, Tops BB, Plasterk RHA, Ketting RF, Hannon GJ (2004) Processing of primary microRNAs by the microprocessor complex. *Nature* 432: 231–235
- Dominguez C, Schubert M, Duss O, Ravindranathan S, Allain FH (2011) Structure determination and dynamics of protein-RNA complexes by NMR spectroscopy. *Prog Nucl Magn Reson Spectrosc* 58: 1–61
- Du Z, Lee JK, Tjhen R, Stroud RM, James TL (2008) Structural and biochemical insights into the dicing mechanism of mouse Dicer: a conserved lysine is critical for dsRNA cleavage. *Proc Natl Acad Sci USA* 105: 2391–2396
- Eckmann CR, Jantsch MF (1997) Xlrpba, a double-stranded RNA-binding protein associated with ribosomes and heterogeneous nuclear RNPs. *J Cell Biol* 138: 239–253
- Fareh M, Yeom KH, Haagsma AC, Chauhan S, Heo I, Joo C (2016) TRBP ensures efficient Dicer processing of precursor microRNA in RNA-crowded environments. *Nat Commun* 9: 13694
- Frank F, Sonenberg N, Nagar B (2010) Structural basis for 5'-nucleotide base-specific recognition of guide RNA by human AGO2. *Nature* 465: 818–822
- Fukunaga R, Han BW, Hung J-H, Xu J, Weng Z, Zamore PD (2012) Dicer partner proteins tune the length of mature miRNAs in flies and mammals. *Cell* 151: 533–546
- Gan J, Tropea JE, Austin BP, Court DL, Waugh DS, Ji X (2006) Structural insight into the mechanism of double-stranded RNA processing by ribonuclease III. *Cell* 124: 355–366
- Gatignol A, Buckler-White A, Berkhout B, Jeang KT (1991) Characterization of a human TAR RNA-binding protein that activates the HIV-1 LTR. *Science* 251: 1597–1600
- Gredell JA, Dittmer MJ, Wu M, Chan C, Walton SP (2010) Recognition of siRNA asymmetry by TAR RNA binding protein. *Biochemistry* 49: 3148–3155
- Gregory RI, Yan K-P, Amuthan G, Chendrimada T, Doratotaj B, Cooch N, Shiekhattar R (2004) The microprocessor complex mediates the genesis of microRNAs. *Nature* 432: 235–240
- Ha T, Selvin PR (2008) *Single-molecule techniques: a laboratory manual*. Cold Spring Harbor, NY: Cold Spring Harbor Laboratory Press
- Haase AD, Jaskiewicz L, Zhang H, Lainé Sé, Sack R, Gatignol A, Filipowicz W (2005) TRBP, a regulator of cellular PKR and HIV-1 virus expression, interacts with Dicer and functions in RNA silencing. *EMBO Rep* 6: 961–967
- Herbert KM, Sarkar SK, Mills M, Delgado De la Herran HC, Neuman KC, Steitz JA (2016) A heterotrimer model of the complete microprocessor complex revealed by single-molecule subunit counting. *RNA* 22: 175–183
- Hoffmann A, Nettels D, Clark J, Borgia A, Radford SE, Clarke J, Schuler B (2011) Quantifying heterogeneity and conformational dynamics from single molecule FRET of diffusing molecules: recurrence analysis of single particles (RASP). *Phys Chem Chem Phys* 13: 1857
- Hutvágner G, McLachlan J, Pasquinelli AE, Bálint E, Tuschl T, Zamore PD (2001) A cellular function for the RNA-interference enzyme Dicer in the maturation of the let-7 small temporal RNA. *Science* 293: 834–838
- Jackson AL, Burchard J, Leake D, Reynolds A, Schelter J, Guo J, Johnson JM, Lim L, Karpilow J, Nichols K, Marshall W, Khvorova N, Linsley PS (2006) Position-specific chemical modification of siRNAs reduces “off-target” transcript silencing. *RNA* 12: 1197–1205
- Jayachandran U, Grey H, Cook AG (2016) Nuclear factor 90 uses an ADAR2-like binding mode to recognize specific bases in dsRNA. *Nucleic Acids Res* 44: 1924–1936
- Jeschke G, Chechik V, Ionita P, Godt A, Zimmermann H, Banham J, Timmel CR, Hilger D, Jung H (2006) DeerAnalysis2006—a comprehensive software package for analyzing pulsed ELDOR data. *Appl Magn Reson* 30: 473–498

- Kawamata T, Seitz H, Tomari Y (2009) Structural determinants of miRNAs for RISC loading and slicer-independent unwinding. *Nat Struct Mol Biol* 16: 953–960
- Khorova A, Reynolds A, Jayasena SD (2003) Functional siRNAs and miRNAs exhibit strand bias. *Cell* 115: 209–216
- Kim VN (2005a) MicroRNA biogenesis: coordinated cropping and dicing. *Nat Rev Mol Cell Biol* 6: 376–385
- Kim VN (2005b) Small RNAs: classification, biogenesis, and function. *Mol Cells* 19: 1–15
- Kim VN, Han J, Siomi MC (2009) Biogenesis of small RNAs in animals. *Nat Rev Mol Cell Biol* 10: 126–139
- Kim Y, Yeo J, Lee JH, Cho J, Seo D, Kim J-S, Kim VN (2014) Deletion of human tarbp2 reveals cellular microRNA targets and cell-cycle function of TRBP. *Cell Rep* 9: 1061–1074
- Kowalinski E, Lunardi T, McCarthy AA, Louber J, Brunel J, Grigorov B, Gerlier D, Cusack S (2011) Structural Basis for the Activation of Innate Immune Pattern Recognition Receptor RIG-I by Viral RNA. *Cell* 147: 423–435
- Kwon SC, Nguyen TA, Choi Y-G, Jo MH, Hohng S, Kim VN, Woo J-S (2016) Structure of human DROSHA. *Cell* 164: 81–90
- Lau P-W, Guiley KZ, De N, Potter CS, Carragher B, MacRae IJ (2012) The molecular architecture of human Dicer. *Nat Struct Mol Biol* 19: 436–440
- Lee HY, Doudna JA (2012) TRBP alters human precursor microRNA processing *in vitro*. *RNA* 18: 2012–2019
- Leuschner PJ, Ameres SL, Kueng S, Martinez J (2006) Cleavage of the siRNA passenger strand during RISC assembly in human cells. *EMBO J* 7: 314–320
- Lingel A, Simon B, Izaurralde E, Sattler M (2003) Structure and nucleic-acid binding of the *Drosophila* Argonaute 2 PAZ domain. *Nature* 426: 465–469
- Lingel A, Simon B, Izaurralde E, Sattler M (2004) Nucleic acid 3'-end recognition by the Argonaute2 PAZ domain. *Nat Struct Mol Biol* 11: 576–577
- López CJ, Oga S, Hubbell WL (2012) Mapping molecular flexibility of proteins with site-directed spin labeling: a case study of myoglobin. *Biochemistry* 51: 6568–6583
- Lund E, Güttinger S, Calado A, Dahlberg JE, Kutay U (2004) Nuclear export of MicroRNA precursors. *Science* 303: 95–98
- Ma J-B, Ye K, Patel DJ (2004) Structural basis for overhang-specific small interfering RNA recognition by the PAZ domain. *Nature* 429: 318–322
- Ma J-B, Yuan Y-R, Meister G, Pei Y, Tuschl T, Patel DJ (2005) Structural basis for 5'-end-specific recognition of guide RNA by the *A. fulgidus* Piwi protein. *Nature* 434: 666–670
- Ma E, Zhou K, Kidwell MA, Doudna JA (2012) Coordinated activities of human Dicer domains in regulatory RNA processing. *J Mol Biol* 422: 466–476
- Masliah G, Barraud P, Allain FH-T (2013) RNA recognition by double-stranded RNA binding domains: a matter of shape and sequence. *Cell Mol Life Sci* 70: 1875–1895
- Matranga C, Tomari Y, Shin C, Bartel DP, Zamore PD (2005) Passenger-strand cleavage facilitates assembly of siRNA into Ago2-containing RNAi enzyme complexes. *Cell* 123: 607–620
- Mello CC, Conte D Jr (2004) Revealing the world of RNA interference. *Nature* 431: 338–342
- Müller BK, Zaychikov E, Bräuchle C, Lamb DC (2005) Pulsed interleaved excitation. *Biophys J* 89: 3508–3522
- Nishida KM, Miyoshi K, Ogino A, Miyoshi T, Siomi H, Siomi MC (2013) Roles of R2D2, a cytoplasmic D2 body component, in the endogenous siRNA pathway in *Drosophila*. *Mol Cell* 49: 680–691
- Noland CL, Ma E, Doudna JA (2011) siRNA repositioning for guide strand selection by human Dicer complexes. *Mol Cell* 43: 110–121
- Noland CL, Doudna JA (2013) Multiple sensors ensure guide strand selection in human RNAi pathways. *RNA* 19: 639–648
- Peters GA, Hartmann R, Qin J, Sen GC (2001) Modular structure of PACT: distinct domains for binding and activating PKR. *Mol Cell Biol* 21: 1908–1920
- Prakash TP, Allerson CR, Dande P, Vickers TA, Sioufi N, Jarres R, Baker BF, Swayze EE, Griffey RH, Bhat B (2005) Positional effect of chemical modifications on short interference RNA activity in mammalian cells. *J Med Chem* 48: 4247–4253
- Rand TA, Petersen S, Du F, Wang X (2005) Argonaute2 cleaves the anti-guide strand of siRNA during RISC activation. *Cell* 123: 621–629
- Ryter JM, Schultz SC (1998) Molecular basis of double-stranded RNA-protein interactions: structure of a dsRNA-binding domain complexed with dsRNA. *EMBO J* 17: 7505–7513
- Schuler B (2007) Application of single molecule Förster resonance energy transfer to protein folding. *Methods Mol Biol* 350: 115–138
- Schwarz DS, Hutvagner G, Du T, Xu Z, Aronin N, Zamore PD (2003) Asymmetry in the assembly of the RNAi enzyme complex. *Cell* 115: 199–208
- Song J-J, Liu J, Tolia NH, Schneiderman J, Smith SK, Martienssen RA, Hannon GJ, Joshua-Tor L (2003) The crystal structure of the Argonaute2 PAZ domain reveals an RNA binding motif in RNAi effector complexes. *Nat Struct Biol* 10: 1026–1032
- Sontheimer EJ (2005) Assembly and function of RNA silencing complexes. *Nat Rev Mol Cell Biol* 6: 127–138
- St Johnston D, Brown NH, Gall JG, Jantsch M (1992) A conserved double-stranded RNA-binding domain. *Proc Natl Acad Sci USA* 89: 10979–10983
- Stalder L, Heusermann W, Sokol L, Trojer D, Wirz J, Hean J, Fritzsche A, Aeschmann F, Pfanzagl V, Basselet P, Weiler J, Hintersteiner M, Morrissey DV, Meisner-Kober NC (2013) The rough endoplasmic reticulum is a central nucleation site of siRNA-mediated RNA silencing. *EMBO J* 32: 1115–1127
- Stefl R, Oberstrass FC, Hood JL, Jourdan M, Zimmermann M, Skrisovska L, Maris C, Peng L, Hofr C, Emeson RB, Allain FH-T (2010) The solution structure of the ADAR2 dsRBM-RNA complex reveals a sequence-specific readout of the minor groove. *Cell* 143: 225–237
- Suzuki HI, Katsura A, Yasuda T, Ueno T, Mano H, Sugimoto K, Miyazono K (2015) Small-RNA asymmetry is directly driven by mammalian Argonautes. *Nat Struct Mol Biol* 22: 512–521
- Takahashi T, Miyakawa T, Zenno S, Nishi K, Tanokura M, Ui-Tei K (2013) Distinguishable *in vitro* binding mode of monomeric TRBP and dimeric PACT with siRNA. *PLoS One* 8: e63434
- Tants J-N, Fesser S, Kern T, Stehle R, Geerloff A, Wunderlich C, Juen M, Hartlmüller C, Böttcher R, Kunzelmann S, Lange O, Kreutz C, Förstemann K, Sattler M (2017) Molecular basis for asymmetry sensing of siRNAs by the *Drosophila* Loqs-PD/Dcr-2 complex in RNA interference. *Nucleic Acids Res* 45: 12536–12550
- Taylor DW, Ma E, Shigematsu H, Cianfrocco MA, Noland CL, Nagayama K, Nogales E, Doudna JA, Wang H-W (2013) Substrate-specific structural rearrangements of human Dicer. *Nat Struct Mol Biol* 20: 662–670
- Tian Y, Simanshu DK, Ma J-B, Park J-E, Heo I, Kim VN, Patel DJ (2014) A phosphate-binding pocket within the Platfor-PAZ-connector helix cassette of human Dicer. *Mol Cell* 53: 606–616
- Tomari Y, Matranga C, Haley B, Martinez N, Zamore PD (2004) A protein sensor for siRNA asymmetry. *Science* 306: 1377–1380
- Tomari Y, Zamore PD (2005) Perspective: machines for RNAi. *Genes Dev* 19: 517–529

- Wang Z, Hartman E, Roy K, Chanfreau G, Feigon J (2011) Structure of a yeast RNase III dsRBD complex with a noncanonical RNA substrate provides new insights into binding specificity of dsRBDs. *Structure* 19: 999–1010
- Wilson RC, Tambe A, Kidwell MA, Noland CL, Schneider CP, Doudna JA (2015) Dicer-TRBP complex formation ensures accurate mammalian microRNA biogenesis. *Mol Cell* 57: 397–407
- Yamashita S, Nagata T, Kawazoe M, Takemoto C, Kigawa T, Güntert P, Kobayashi N, Terada T, Shirouzu M, Wakiyama M, Muto Y, Yokoyama S (2011) Structures of the first and second double-stranded

RNA-binding domains of human TAR RNA-binding protein. *Protein Sci* 20: 118–130

- Yang SW, Chen H-Y, Yang J, Machida S, Chua N-H, Yuan YA (2010) Structure of *Arabidopsis* HYPONASTIC LEAVES1 and its molecular implications for miRNA processing. *Structure* 18: 594–605



License: This is an open access article under the terms of the Creative Commons Attribution 4.0 License, which permits use, distribution and reproduction in any medium, provided the original work is properly cited.

Appendix Supplementary Information

Structural basis of siRNA recognition by TRBP double-stranded RNA binding domains

Authors

Gregoire Masliah¹, Christophe Maris¹, Sebastian L.B. König², Maxim Yulikov³, Florian Aeschimann⁴, Anna L. Malinowska⁵, Julie Mabile⁴, Jan Weiler⁴, Andrea Holla², Juerg Hunziker⁴, Nicole Meisner-Kober⁴, Benjamin Schuler², Gunnar Jeschke³, Frederic H.-T. Allain¹

Affiliations

¹Institute of Molecular Biology and Biophysics, ETH Zürich, CH-8093 Zürich, Switzerland

²University of Zürich, Department of Biochemistry, Winterthurerstrasse 190, CH-8057 Zürich, Switzerland

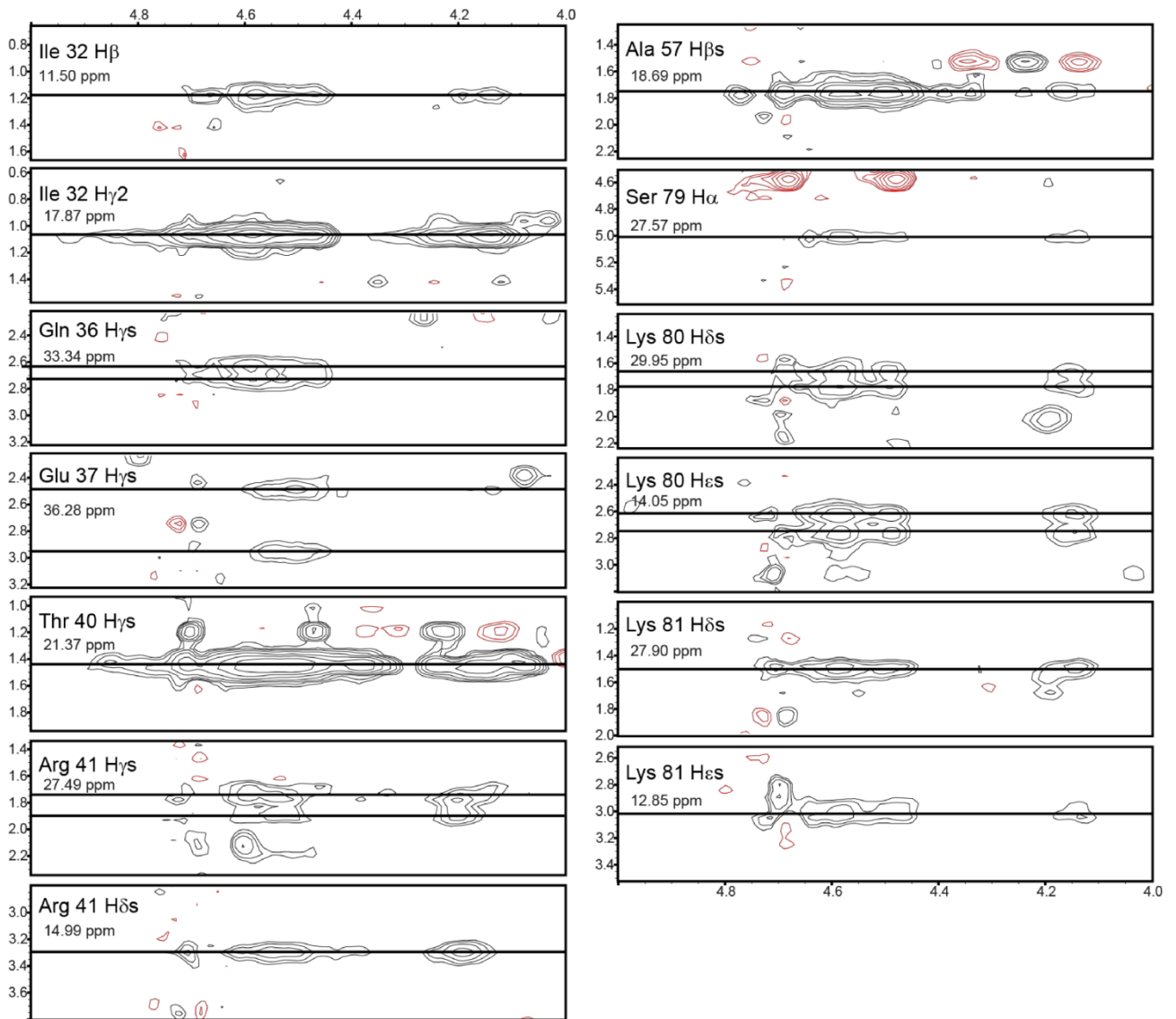
³Laboratory of Physical Chemistry, ETH Zürich, CH-8093 Zürich, Switzerland

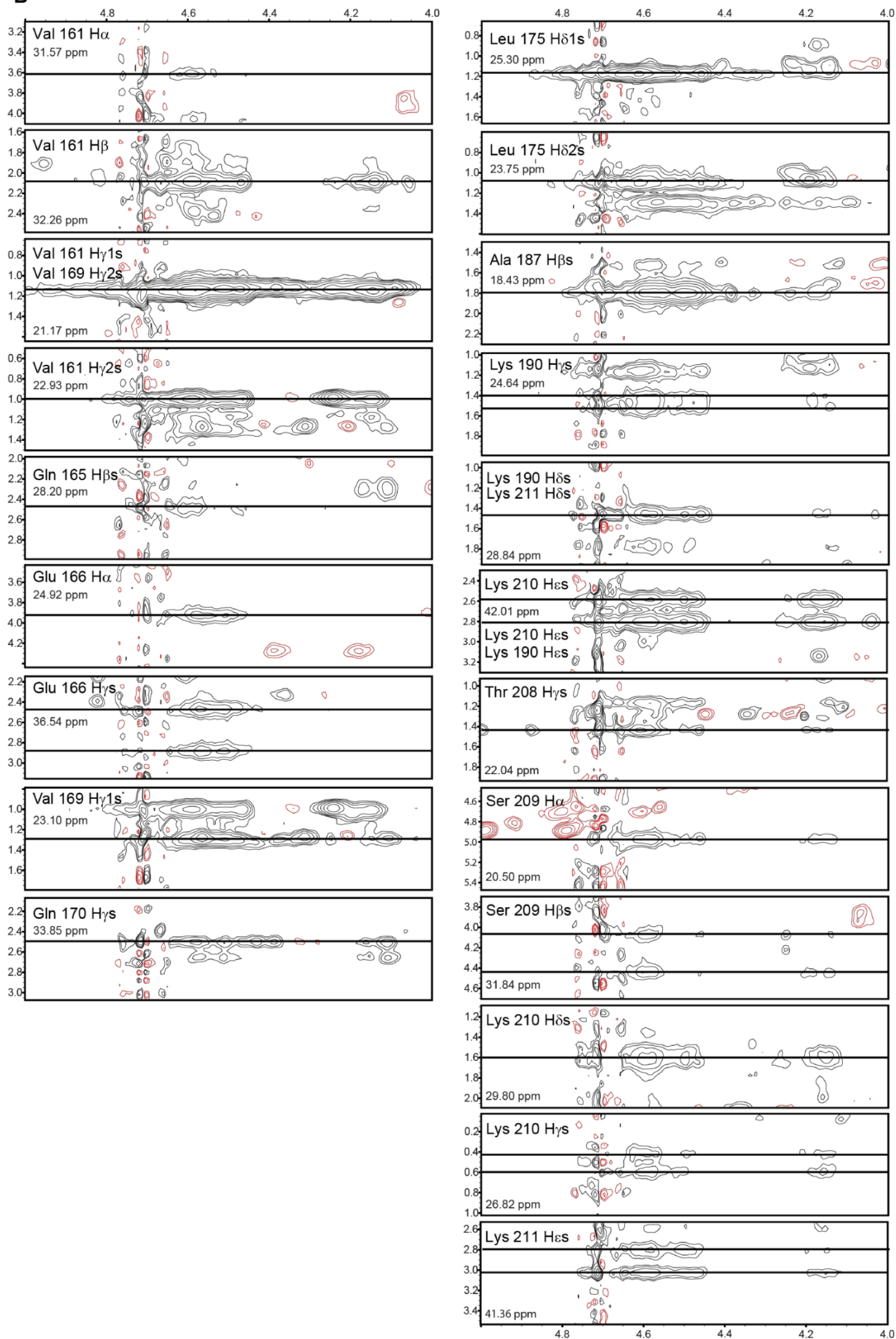
⁴Novartis Institutes for Biomedical Research, CH-4000 Basel, Switzerland

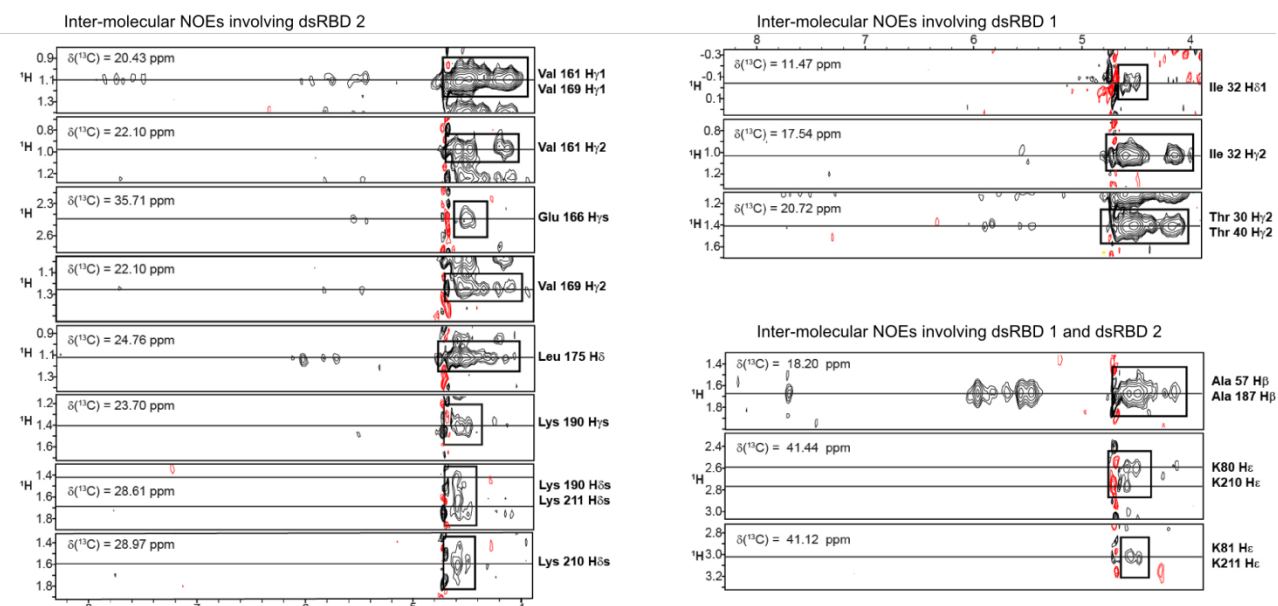
⁵Institute of Pharmaceutical Sciences, Department of Chemistry and Applied Biosciences, ETH Zürich, CH-8093 Zürich, Switzerland.

Correspondence: allain@mol.biol.ethz.ch

Page	Description
A2	Appendix Figure S1
A5	Appendix Table S1
A6	Appendix Table S2
A7	Appendix Table S3
A8	Appendix Methods
A16	Appendix References

A

B

C

Appendix Figure S1. Selected regions of ¹³C-edited-filtered NOESY spectra showing protein-RNA intermolecular NOEs observed in (A) the dsRBD1-EL86 complex, (B) the dsRBD2-EL86 complex, and (C) the dsRBD12-EL86 complex. The protein residue and proton involved in each intermolecular NOE are indicated on the right side the spectrum strips. The spectral window displayed in (A) and (B) corresponds to RNA H4'/H5'/H5'', and to H6/H8/H2/H1'/H4'/H5'/H5'' in (C).

NMR statistics of the structures of individual TRBP dsRBDs in dsRNA bound state ^{a,b}		
	dsRBD1	dsRBD2
<i>NMR restraints</i>		
Total NOE	945	1355
Intra-residue	200	318
Sequential (i - j = 1)	114	340
Medium range (1 < i - j < 5)	198	287
Long-range (i - j > 5)	433	410
Torsion angles ^c	126	96
Residual Dipolar Couplings ^d	44	217
<i>Structure statistics</i>		
Violations (mean ± SD)		
Distance restraints violations > 0.3 Å	1.2 ± 0.7	0.5 ± 0.5
Max. distance restraints violation (Å)	0.34 ± 0.05	0.31 ± 0.03
Dihedral angle violation > 5°	0.7 ± 0.6	0.0 ± 0.0
Max. dihedral angle violation (°)	6.3 ± 2.1	1.6 ± 0.9
RDC r.m.s.d.	1.0 ± 0.1	2.4 ± 0.1
Q-factor	0.05 ± 0.04	0.22 ± 0.00
<i>Deviations from idealized geometry</i>		
Bond lengths (Å)	0.0037 ± 0.0000	0.0038 ± 0.0000
Bond angles (°)	1.698 ± 0.013	1.538 ± 0.013
<i>R.m.s.d. from averaged structure^e (Å)</i>		
Backbone	0.35 ± 0.11	0.22 ± 0.05
Heavy atoms	0.74 ± 0.08	0.81 ± 0.08
<i>Ramachandran analysis</i>		
Most favored regions (%)	93.5 ± 1.3	94.6 ± 1.2
Additionally allowed regions (%)	6.2 ± 1.0	5.4 ± 1.2
Generously allowed regions (%)	0.1 ± 0.3	0.0 ± 0.0
Disallowed regions (%)	0.2 ± 0.5	0.0 ± 0.0

Appendix Table S1.

- a.** NMR spectra were acquired on samples with a protein-RNA stoichiometry of 1:2.
- b.** All statistics were calculated on an ensemble of 20 structures of lowest energy.
- c.** Dihedral angle restraints were obtained with the program TALOS+ + [Shen et al. 2009].
- d.** dsRBD1 dataset consisted of 36 (NH) RDCs only. DsRBD2 dataset consisted of 55 (NH), 59 (CαC), 51 (HC), and 52 (NC) RDCs.
- e.** Structures from dsRBD1 and dsRBD2 ensembles were superposed, using residues 18-97 and 160-226, respectively.

Statistics on RDCs collected in the dsRBD12 - EL86 complex				
	Rp^a	r.m.s.d.	Da (Hz)	Rh
Individual domains^b				
rbd 1	0.93±0.02	4.24±0.67	10.33±0.48	0.25±0.05
rbd 2	0.95±0.02	3.41±0.58	10.84±0.44	0.29±0.05
Two domains antiparallel^c				
12,13^d	0.71±0.02	8.0±0.2	-1.15±6.04	0.61±0.04
13,14^d	0.83±0.02	6.2±0.4	7.99±0.4	0.39±0.05
14,15^d	0.93±0.02	4.1±0.5	10.44±0.19	0.25±0.03
15,16^d	0.84±0.03	6.2±0.6	9.33±0.44	0.31±0.06
Two domains parallel^c				
37,38^d	0.93±0.01	4.1±0.4	10.35±0.31	0.27±0.04
38,39^d	0.87±0.02	5.6±0.4	8.26±0.36	0.29±0.04
39,40^d	0.71±0.03	8.0±0.3	1.34±5.71	0.59±0.05

Appendix Table S2.

- a.** Pearson's correlation factor between experimental and back-calculated RDCs
- b.** All values were calculated using the NMR structures of the single domains in their RNA bound form.
- c.** All values were calculated using three-dimensional models of dsRBD12-EL86 complexes obtained by keeping dsRBD2 at a fixed position while shifting dsRBD1 position systematically.
- d.** Sequence number of the RNA residue flanking Ala 57 methyl group (dsRBD1-loop 2).

Appendix Table S3. NMR statistics of the dsRBD12 - EL86 structure ensembles A and B

Structures of dsRBD12 – EL86 complex ^{a,b}			
<i>NMR restraints</i>	dsRBD1	dsRBD2	EL86
Total NOE	945	1355	268
Intra-residue	200	318	168
Sequential (i - j = 1)	114	340	120
Medium range (1 < i - j < 5)	198	287	0
Long-range (i - j > 5)	433	410	0
Hydrogen bonds	0	0	70
Intermolecular NOE	14	30	
Torsion angles ^c	126	96	240
Residual Dipolar Couplings ^d	44	217	0
<i>Structures statistics</i>	Ensemble A	Ensemble B	
Violations (mean ± SD)			
Distance restraints violations > 0.4 Å	1.2 ± 0.8	0.5 ± 0.7	
Max. distance restraint violation (Å)	0.50 ± 0.11	0.39 ± 0.05	
Dihedral angle violation > 5°	4.8 ± 1.6	4.6 ± 1.0	
Max. dihedral angle violation (°)	12.3 ± 9.3	9.1 ± 2.1	
RDC r.m.s.d.	0.9 ± 0.1 / 3.1 ± 0.2	0.9 ± 0.1 / 3.1 ± 0.1	
Q-factor	0.04 ± 0.01 / 0.29 ± 0.02	0.04 ± 0.01 / 0.29 ± 0.01	
<i>Deviations from idealized geometry</i>			
Bond lengths (Å)	0.0037 ± 0.0000	0.0037 ± 0.0000	
Bond angles (°)	1.845 ± 0.009	1.847 ± 0.007	
<i>Structural r.m.s.d.^e (Å)</i>			
Backbone	0.85 ± 0.13	0.88 ± 0.20	
Heavy atoms	1.19 ± 0.11	1.25 ± 0.16	
<i>Ramachandran analysis</i>			
Most favored regions (%)	91.8 ± 1.1	93.0 ± 1.0	
Additionally allowed regions (%)	7.1 ± 0.9	5.9 ± 0.8	
Generously allowed regions (%)	0.7 ± 0.6	0.5 ± 0.6	
Disallowed regions (%)	0.4 ± 0.6	0.6 ± 0.6	

a. NMR spectra were acquired on samples with a protein-RNA stoichiometry of 1:2.

b. All statistics were calculated on an ensemble of 20 structures of lowest energy.

c. Dihedral angle restraints for dsRBD1 and dsRBD2 were obtained with the program TALOS+ [Shen et al. 2009]. Standard values for a A-form RNA double helix were used for EL86.

d. DsRBD1 dataset consisted of 36 (NH) RDCs only. DsRBD2 dataset consisted of 55 (NH), 59 (CaC), 51 (HC), and 52 (NC) RDCs.

e. Structures from ensembles A and B were superposed, using residues 18-97 (dsRBD1), 160-225

(dsRBD2), and 1-19, 22-40 (EL86). Structures in complexes A and B were superposed on structures 10 and 17, respectively

Appendix Supplementary Methods

Structure calculation

Protein backbone and side chain resonance assignments were obtained from triple resonance spectra (HNCACB, CBCA(CO)NH, and HNCO) and TOCSY spectra (H(CCO)NH and (H)C(CO)NH), respectively. Inter proton distance restraints were extracted for each domain (dsRBD1 and dsRBD2) from 3D ^{13}C -edited NOESY-HSQC and 3D ^{15}N -edited NOESY-HSQC measured on dsRBD1-EL86 and dsRBD2-EL86 complexes (120 ms mixing times). Residual Dipolar Couplings (RDCs) were derived from the difference of peak splitting observed under isotropic and anisotropic (10 mg.mL⁻¹ Pf1 phages (ASLA biotech) conditions. The set of RDCs used to orient dsRBD1 and dsRBD2 with respect to each other was measured on the dsRBD12-EL86 complex. Aromatic-aromatic, sugar-aromatic and imino-imino NOE cross peaks observed in NOESY spectra recorded on EL86 were typical of those found in A-form RNA structures [Buuren et al., 1998; Wüthrich 1986] The two uracils at both 3'overhangs were flexible as indicated by the intense H5-H6 correlations in TOCSY spectrum (data not shown). The NOE pattern typical of an A-form RNA and the flexibility of the nucleotides at both 3' overhangs remained unchanged upon protein binding. Based on these data we used both inter proton distance and dihedral restraints to constraint EL86 to an A-form RNA helix. Protein chemical shifts and NOESY spectra were used as input to the programs ATNOS-CANDID [Herrmann et al., 2002] and CYANA [Güntert 2004]. Structures were further refined with the AMBER 12 package [Case et al.] using a standard simulated-annealing protocol. *Residual Dipolar Coupling (RDC) analysis.* The fourteen structural models of the dsRBD12-EL86 complex used to analyze RDCs, were calculated with the program CYANA and a combination of experimental and artificial structural constraints. The two dsRBDs were folded using experimental distance restraints and RDCs collected on the single domains in complex with EL86, EL86 was folded using inter proton and backbone dihedral restraints with standard values for a A-form RNA double helix (Supplementary Methods), dsRBD1 and dsRBD2 were positioned on EL86 using inter proton distance restraints. The RNA residues and the protein

side chains involved in these restraints were selected on the basis of inter molecular NOEs. The set of RNA residues serving as docking points for each dsRBD was changed consistently for each model in order to preserve dsRBD's canonical dsRNA binding mode. The agreement of each model with a set of RDCs measured on the dsRBD12-EL86 complex was estimated by calculating the r.m.s.d. and the Pearson correlation factor

For each model, the r.m.s.d. and the Pearson correlation factor between calculated and experimental RDCs were calculated with the program PALES [Zweckstetter 2008].

Protein purification

E.coli BL21(DE3) Codon-plus (RIL) cells were transformed with pet28a vectors allowing the expression of proteins fused to a polyhistidine affinity tag at the N-terminus. The pet28a plasmids were engineered to encode a TEV cleavage site between the polyhistidine affinity tag and the multicloning site. Cells were grown in LB medium or M9 medium supplemented with ¹³C-labeled glucose and / or ¹⁵NH₄Cl (for isotopically labeled samples) at 37 °C to a cell density of 0.6 a.u. (OD₆₀₀). Protein expression was induced by addition of 0.5 mM of isopropyl-β-D-thiogalactopyranoside, temperature was cooled down to 30 °C, cells were harvested after 12-16 hours and resuspended in buffer A (50 mM Tris-HCl [pH 8.0], 1 M NaCl, 7 mM β-mercaptoethanol, 10 mM imidazole, 0.1% Triton 100X) and lysed by sonication. The lysate was clarified by centrifugation (30,000 × g, 40 min at 4 °C), the supernatant was loaded on a column prepacked with Ni-NTA beads (GE Healthcare) previously equilibrated with buffer A. The proteins were eluted with a linear gradient of buffer B (50 mM Tris-HCl [pH 8.0], 1 M NaCl, 7 mM β-mercaptoethanol, 1 M imidazole). The fractions containing the protein were pooled and dialyzed overnight at 4 °C against buffer C (20 mM NaPO₄ [pH 6.4], 7 mM β-mercaptoethanol). Precipitate was discarded by centrifugation. Polyhistidine tags were cleaved off with in-house TEV protease (1 OD₂₈₀ per 100 OD₂₈₀ of substrate, overnight at 4°C), uncleaved products were removed by further processing the samples through Ni-NTA beads. As a final purification step, samples were applied on a Superdex

200pg 16×60 column (GE Healthcare) equilibrated with NMR buffer (20 mM NaPO₄ [pH 6.4], 5 mM DTT). Protein-containing fractions were pooled and concentrated to 1.5 mM and stored at -20 °C until further use.

For single-molecule FRET experiments, the codon-optimized sequence of TRBP 22-235 with amino acid exchanges C73A/M100C/C196V and a threonine insertion between C158 and N159 was cloned into a pET47b(+)-based vector. Site-directed mutagenesis was performed to create single-cysteine variants at position 100 (dsRBD12 M100C/C158S) and position 158 (dsRBD12 M100S). For fluorescence labeling, maleimide-functionalized CF660R (Biotium, Inc., Fremont, CA) dissolved in anhydrous DMSO was added in 3-fold excess to purified protein solution. The coupling reaction was allowed to proceed overnight at 8°C, followed by quenching with 10 mM DTT. Free dye and DTT were removed using a HiTrap Desalting column (GE Healthcare Bio-Sciences AG, Uppsala, Sweden). Finally, singly-labeled dsRBD12 variants were separated from unlabeled species by cation-exchange chromatography (MonoS 5/50 GL, GE Healthcare Bio-Sciences AG, Uppsala, Sweden). To generate donor-acceptor labeled dsRBD12, maleimide-functionalized CF660R was added at a molar ratio of 1:0.7 (protein:dye). The reaction was performed and quenched as described above, followed by separation of singly labeled TRBP from unlabeled and doubly labeled protein by cation-exchange chromatography. Subsequently, maleimide-functionalized Cy3b was added at a molar ratio of 1:3 (protein:dye). The coupling reaction was conducted as described above and doubly labeled TRBP purified by cation-exchange chromatography. For all proteins, sample quality and chromophore incorporation were confirmed by electrospray ionization mass spectrometry.

EPR Spectroscopy

Nitroxide–nitroxide distance measurements were performed with the four-pulse DEER experiment [Pannier et al., 2000] at Q band (34–36 GHz) at 50 K on home-built EPR spectrometer [Gromov et al., 2001] with a rectangular cavity allowing oversized samples [Tschaggelar et al.

2009]. The chosen DEER measurements temperature of 50 K corresponds approximately to the optimum measurement conditions with respect to the longitudinal and transverse relaxation of nitroxide radicals. The sample temperature was stabilized with a He-flow cryostat (ER 4118 CF, Oxford Instruments).

The previously reported optimal settings were used in the DEER measurements [Polyhach et al., 2012]. In brief, all pulses were set to a duration of 12 ns. The offset between pump and detection frequencies was set to $f_{det} - f_{pump} = -100\text{MHz}$. The first inter-pulse delay time in the DEER sequence was set to 400 ns in all cases. The second delay time (between the primary echo and the refocusing pulse) was set according to the length of the DEER trace required to provide sufficient range for background correction. Typical measurement time was 5–20 h depending on the length of the DEER trace, and actual dipolar modulation depth.

Fitting of DEER data was performed with DeerAnalysis 2009 software [Jeschke et al. 2006]. To avoid possible artefacts, the range for the background fit was cut at least 100 ns before the end of the DEER trace. All traces were fitted with the unrestricted distance distribution model. In each case Tikhonov regularization [Jeschke et al., 2004; Chiang et al., 2005] was performed and distributions corresponding to different regularization parameters were analyzed. A 3D background model was assumed in the background fits for all samples. In all cases, the obtained distance distribution was stable with respect to the change of the background model.

RNA synthesis and labeling

Single-molecule FRET experiments: EL86 oligonucleotides were purchased RP-HPLC-purified from Integrated DNA Technologies BVBA (Leuven, Belgium), where EL86up (5'-UUA AUU AUC UAU UCC GUA CUU-3') was functionalized with a biotin at its 3'-end, while a primary amino modifier was incorporated at the 3'-end of EL86down (5'-GUA CGG AAU AGA UAA UUA AUU-3'). For both sequences, the purity was confirmed by analytical RP-HPLC, followed by fluorescently labeling EL86down with *N*-hydroxysuccinamide-functionalized Cy3B (GE

Healthcare, Glattbrugg, Switzerland) [Greenfeld & Herschlag 2013]. Cy3B-labelled EL86down was EtOH-precipitated to remove free dye, followed by preparative RP-HPLC purification and lyophilization. Successful incorporation of Cy3B was confirmed by MALDI-MS. All RNA sequences were dissolved in nuclease-free H₂O (Applichem GmbH, Darmstadt, Germany) and stored at -20 °C at a concentration of 100 μM until further use. *NMR and EPR experiments:* EL86 antisense (5'-UUA AUU AUC UAU UCC GUA CUU-3') and sense (5'-GUA CGG AAU AGA UAA UUA AUU-3') strands were synthesized on an Äkta Oligopilot plus OP100 (*GE Healthcare*) with a 12 mL column reactor (*GE Healthcare*, order no. 18-1101-16) using a solid-phase synthesis cyclic procedure consisting of 5 steps, based on the manufacturer's template method. Base-protected ribonucleoside phosphoramidites were dissolved in anhydrous acetonitrile under argon to a concentration of 0.15 M. Activated molecular sieves were added to each amidite solution and the bottles were left to stand overnight. The following synthesis cycle applied: First, the 4,4'-dimethoxytrityl (DMT) protecting group was removed by adding deblocking reagent (3% DCA in toluene, *Merck*, order no. BI0832). Coupling was then achieved by adding the phosphoramidite solution (1.9 eq.) to the column along with an equal volume of 0.5M 5-ethylthiotetrazole (*ChemGenes*, order no. RN-6397) in acetonitrile. Coupling was followed by capping by adding Cap A (*Biosolve*, order no. 036124, 2-methylimidazole / acetonitrile 1:4 (v/v)) and Cap B, obtained by mixing equivalent amounts of Cap B1 (*Biosolve*, order no. 037424, acetic anhydride / acetonitrile 2:3 (v/v)) and Cap B2 (*Biosolve*, order no. 037425, pyridine / acetonitrile 3:2 (v/v)). The oligonucleotide was subsequently oxidized by adding iodine (*Biosolve*, order no. 150724, 0.05M iodine in pyridine/water 9:1 (v/v)). The column was washed between each step with anhydrous acetonitrile. The synthesis procedure ended with a final detritylation step in order to remove the last DMT-group, allowing for easier purification. After completion of synthesis, the column was placed under vacuum in order to remove all remaining acetonitrile, and the support was transferred into a glass vial.

The oligonucleotide was cleaved from the support and deprotected by first incubating the support in a

glass bottle with 19 mL concentrated aqueous methylamine at 35°C for 45 min under gentle agitation. Then the flask was cooled in an ice bath and the solid support filtered off over a sintered glass funnel. The support was washed with DMSO (3 x 10 mL). The filtrate was cooled in an ice bath and 15 mL triethylamine-trishydrofluoride was added slowly under shaking. The solution was heated to 50°C for 60 min and then cooled again in an ice bath. When cold, 64 mL of a 50 mM sodium acetate buffer (pH=5.2) was added.

The oligonucleotide was purified on a Fineline pilot 35 column (*GE Healthcare*, order no. 18-1102-02) filled with TSK Gel SuperQ-5PW ion exchange resin (*Tosoh*, order no. 18546) using an ÄKTAexplorer (*GE Healthcare*). Buffer A: 20 mM aqueous sodium phosphate, pH = 7.0; buffer B: 20 mM aqueous sodium phosphate, pH = 7.0, 1M NaCl; gradient: 20 – 80% B in 43 column volumes; flow rate 30 mL / min; column heated to 63°C. Fractions of appropriate purity were pooled and then desalted by tangential flow filtration (TFF) on a Minim II TFF system (*Pall Corporation*) using a 1K Omega Centramate T-Series filtration unit (*Pall Corporation*, order no. OS001T12). The oligonucleotide was filtered on a Steriflip-GP filtration unit (*Millipore*, order no. SCGP00525) and the quality of the oligonucleotide verified by HPLC and UPLC-MS before lyophilization.

Analytical ion-exchange HPLC was performed on an *Agilent* 1200 Series HPLC with a Dionex DNAPac® PA200 analytical column (4 x 250 mm). Buffer A: 10 mM NaClO₄, 10 mM Tris-HCl, 20% EtOH; buffer B: 300 mM NaClO₄, 10 mM Tris-HCl, 20% EtOH; flow rate: 1mL/min; column temperature: 80°C; gradient: 40 – 60% B in 7 min.

UPLC-MS chromatography analysis was performed on an Acquity UPLC / LCT Premier XE ES mass spectrometer (*Waters*) with an Acquity UPLC® BEH C18 1.7 µm 2.1 x 50 mm column. Buffer A: triethylamine (32 mM); hexafluoroisopropanol (100 mM) in water; buffer B: 20% buffer A, 80% MeOH; flow rate: 0.25 mL/min; column temperature: 15°C; gradient: 5 – 60% B in 3.75 min.

mRNA knockdown assay

Transfection of HeLa cells with siRNAs. The human HeLa YFP cells were maintained in 5 % humidified CO₂ atmosphere at 37 °C in antibiotics free DMEM medium (Invitrogen, #21063) supplemented with + 10% FCS (heat-inactivated) and + 1% L-Glu designated as growth medium. After reaching an 80 % subconfluent stage, one day before transfection, cells were harvested by trypsinization and finally seeded in 150 µl DMEM growth medium at a density of 4000 cells/well into black 96-well assay plates (Corning Costar, clear bottom, #3606) and incubated in a 5 % humidified CO₂ atmosphere at 37 °C. After overnight incubation, the cells were transfected with siRNA-HiPerFect complex. Briefly, HiPerFect and siRNA were pre-diluted in OptiMEM. The siRNA-HiPerFect mixture (18.3 nM siRNA, 0.450 µl HiPerFect in 65.45 µl) were pre-incubated for 18 minutes to form the siRNA-HiPerFect complex. Just before adding the complex, 50 µl of medium were removed. 50 µl of complex and 25 µl DMEM containing 30% of FCS was sequentially added to the cells to obtain the final concentration of 6 nM of siRNA. After transfection, cells were incubated for ca. 30 hrs at 37 °C. *Cell lysis and RT-qPCR analysis.* After the removal of the medium, the cells were washed with 125 µl FCW buffer / well (included in FastLane Cell Multiplex Kit, Qiagen, # 216513). Afterwards the cells were either shock frozen on dry ice and transferred to the -80 °C freezer or directly lysed. For the lysis, cells were treated for 10 minutes with the FastLane processing mix (47 µl FCPL / well + 3 ul gDNA wipeout buffer 2 / well). Carefully, 40 ul of the Lysate were transferred to a new plate to perform a heat inactivation step (6 min at 75 °C). Afterwards the lysate was diluted 1:5 in RNase free water. One-step Duplex real-time PCR was performed using Fastlane Cell Multiplex kit (Qiagen #216513) and QuantiTect Multiplex RT-PCR kit (Qiagen #204643). Relative quantification was carried out on the ABI PRISM 7900 using Taqman gene expression assays from Applied Biosystems: hs ELAVL1_FAM_Hs00171309_m1 and an Endogenous Control of hs HPRT1_VIC_4326321E. The raw data of the Ct value were transferred into an excel template automatically by using the file load software 3.0.11. The transfection of all siRNAs were independently repeated on two assay plates. Positive

control siRNAs treatments targeting eYFP were done in triplicate on each plate. The eYFP knock down serves as a transfection control which reaches the threshold. The mean values of the two plates are presented as percent of YFP-siRNA control (serves as a kind of target-siRNA untreated control). The relative gene expression was analyzed using the delta-delta-Ct method.

Appendix Supplementary References

Buuren, B.N.M. and Wijmenga, S.S. (1998) *The use of NMR methods for conformational studies of nucleic acids. Progr. NMR Spectrosc. 32: 287–387*

Case, D., Darden, T., Cheatham III, T., Simmerling, C., Wang, J., Duke, R., Luo, R., Walker, R., Zhang, W., Merz, K. and others (). AMBER 12, University of California: San Francisco, 2012.

Chiang, Y.-W., Borbat, P. P. and Freed, J. H. (2005). *The determination of pair distance distributions by pulsed ESR using Tikhonov regularization.*, J Magn Reson 172 : 279-295.

Greenfeld, M, Herschlag, D. (2013), Methods Enzymol. 2013;530:281-97. doi: 10.1016/B978-0-12-420037-1.00015-4.

Gromov, I., Shane, J., Forrer, J., Rakhmatoullin, R., Rozentzwaig, Y. and Schweiger, A. (2001). *A Q-band pulse EPR/ENDOR spectrometer and the implementation of advanced one- and two-dimensional pulse EPR methodology.*, J Magn Reson 149 : 196-203.

Güntert, P. (2004). *Automated NMR structure calculation with CYANA.*, Methods Mol Biol 278 : 353-378.

Herrmann, T., Güntert, P. and Wüthrich, K. (2002). *Protein NMR structure determination with automated NOE-identification in the NOESY spectra using the new software ATNOS.*, J Biomol NMR 24 : 171-189.

Hoffmann, A., Nettels, D., Clark, J., Borgia, A., Radford, S. E., Clarke, J. and Schuler, B. (2011). *Quantifying heterogeneity and conformational dynamics from single molecule FRET of diffusing molecules: recurrence analysis of single particles (RASP)*, Phys. Chem. Chem. Phys. 13 : 1857.

Jeschke, G., Panek, G., Godt, A., Bender, A. and Paulsen, H. (2004). *Data analysis procedures for pulse ELDOR measurements of broad distance distributions*, Appl. Magn. Reson. 26 : 223-244.

Jeschke, G., Chechik, V., Ionita, P., Godt, A., Zimmermann, H.; Banham, J.; Timmel, C. R.; Hilger, D. and Jung, H. (2006). *DeerAnalysis2006textemdasha comprehensive software package for analyzing pulsed ELDOR data*, Appl. Magn. Reson. 30 : 473-498.

Müller, B. K., Zaychikov, E., Bräuchle, C. and Lamb, D. C. (2005). *Pulsed interleaved excitation.*, Biophys J 89 : 3508-3522.

Pannier, M., Veit, S., Godt, A., Jeschke, G. and Spiess, H. W. (2000). *Dead-time free measurement of dipole-dipole interactions between electron spins.*, J Magn Reson 142 : 331-340.

Polyhach, Y., Bordignon, E., Tschaggelar, R., Gandra, S., Godt, A. and Jeschke, G. (2012). *High sensitivity and versatility of the DEER experiment on nitroxide radical pairs at Q-band frequencies.*, Phys Chem Chem Phys 14 : 10762-10773.

Shen, Y., Delaglio, F., Cornilescu, G., and Bax, A. (2009). *TALOS+: A hybrid method for predicting protein backbone torsion angle from NMR chemical shifts.*, J. Biomol . NMR 44 : 213-223.

Schuler, B. (2007). *Application of single molecule Förster resonance energy transfer to protein*

folding., Methods Mol Biol 350 : 115-138.

Tschaggelar, R., Kasumaj, B., Santangelo, M. G., Forrer, Jö., Leger, P., Dube, H., Diederich, F., Harmer, J., Schuhmann, R., García-Rubio, I. and Jeschke, G. (2009). *Cryogenic 35GHz pulse ENDOR probehead accommodating large sample sizes: Performance and applications.*, J Magn Reson 200 : 81-87.

Wüthrich, K. (1986) *NMR of proteins and nucleic acids.* John Wiley & Sons, New York

Zweckstetter, M. (2008) *NMR: prediction of molecular alignment from structure using the PALES software.*, Nat. Protoc. 3 : 679-690.

Expanded View Figures

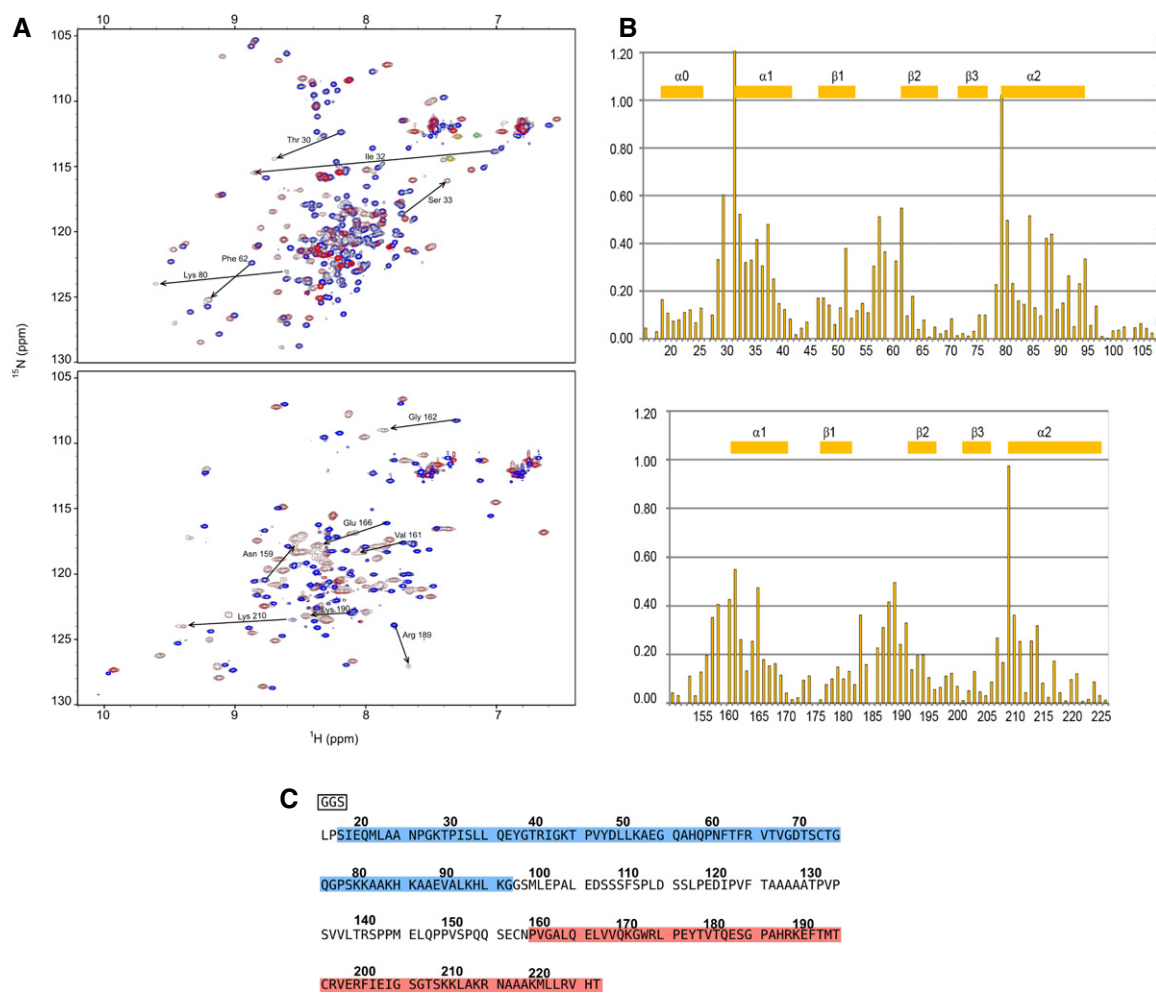


Figure EV1. Mapping of chemical shift perturbations occurring upon the formation of dsRBD1-EL86 and dsRBD2-EL86 complexes. DsRBD12 amino-acid sequence.

- A ^{15}N -HSQC overlays of dsRBD-1 (upper) and dsRBD-2 (lower) in the free state (blue) and bound to dsRNA (red). Largest chemical shift perturbations observed upon EL86 binding are indicated with arrows.
- B Chemical shift perturbations mapping onto the primary structures of dsRBD-1 (upper) and dsRBD-2 (lower). Gaps correspond to proline residues. Secondary structure is indicated for each domain.
- C Amino acid sequence of TRBP dsRBD12. The "GGGS" stretch in the black frame is coming from the expression vector. DsRBD1 (dsRBD2) regions are highlighted in blue (red).

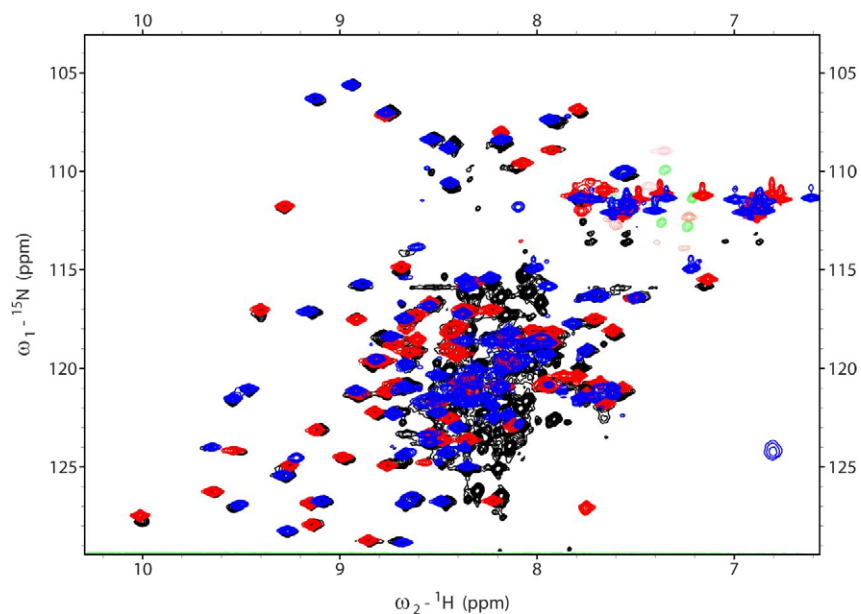


Figure EV2. Overlay of EL86-bound dsRBD1, dsRBD2, and dsRBD12 fingerprints.

The ^{15}N -HSQC spectra of dsRBD1, dsRBD2, and dsRBD12, are shown in blue, red, and black, respectively. All three spectra were recorded in the presence of dsRNA (EL86). Unmatched black peaks correspond to the residue linker between dsRBD1 and dsRBD2.

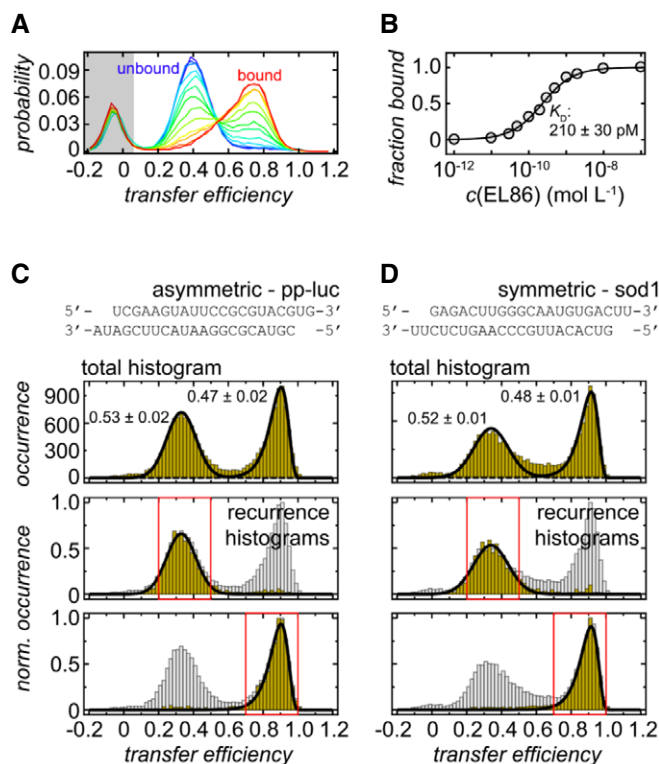


Figure EV3. TRBP-RNA binding isotherm and sequence dependence of RNA binding as characterized by single-molecule FRET.

- A** Normalized transfer efficiency histograms of Cy3B-CF660R-labeled dsRBD12 in the presence of different EL86 RNA concentrations. Free dsRBD12 (blue) can be distinguished from RNA-bound dsRBD12 (red) via its transfer efficiency. The peak in the gray-shaded area originates from molecules without an active acceptor fluorophore and is not included in the analysis.
- B** RNA binding curve generated from the plots shown in panel (A). The experimental data were fitted to a binding isotherm (solid line).
- C, D** Transfer efficiency histograms of CF660R-labeled dsRBD12_22-235 C158S in complex with Cy3B-labeled pp-luc and sod1. Top: Transfer efficiency histograms reveal two subpopulations that are equally populated. Errors associated with their estimates from multiple measurements. Bottom: Recurrence transfer efficiency histograms (Hoffmann *et al*, 2011) were used to extract subpopulation-specific fit parameters for the peak shapes. Red boxes highlight the initial transfer efficiency range used for the analysis. The recurrence interval T was set to (0, 10 ms). See Materials and Methods section for details.

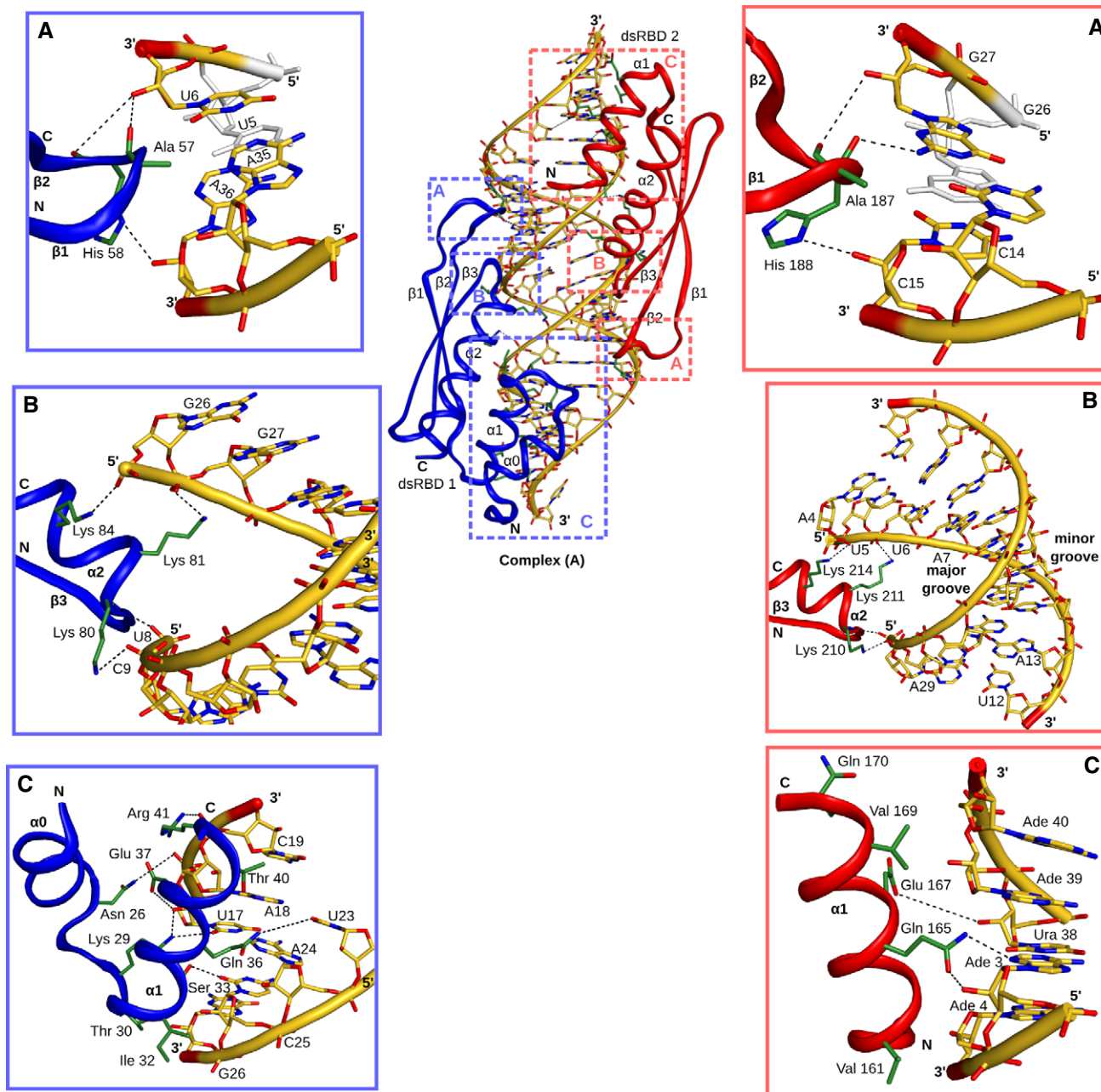


Figure EV4. Interactions between dsRBD12 and EL86.

A–C A representative structure of complex A is shown with dsRBD1 and dsRBD2 colored in blue and red, respectively. Protein side-chains and RNA are represented as green and yellow sticks, respectively. Polar interactions are displayed with dashes. The interactions between EL86 and the β 1– β 2 loop, KKxAK motif, and helix α 1 of dsRBD1 (blue) and dsRBD2 (red), are shown in details in panels (A–C), respectively.

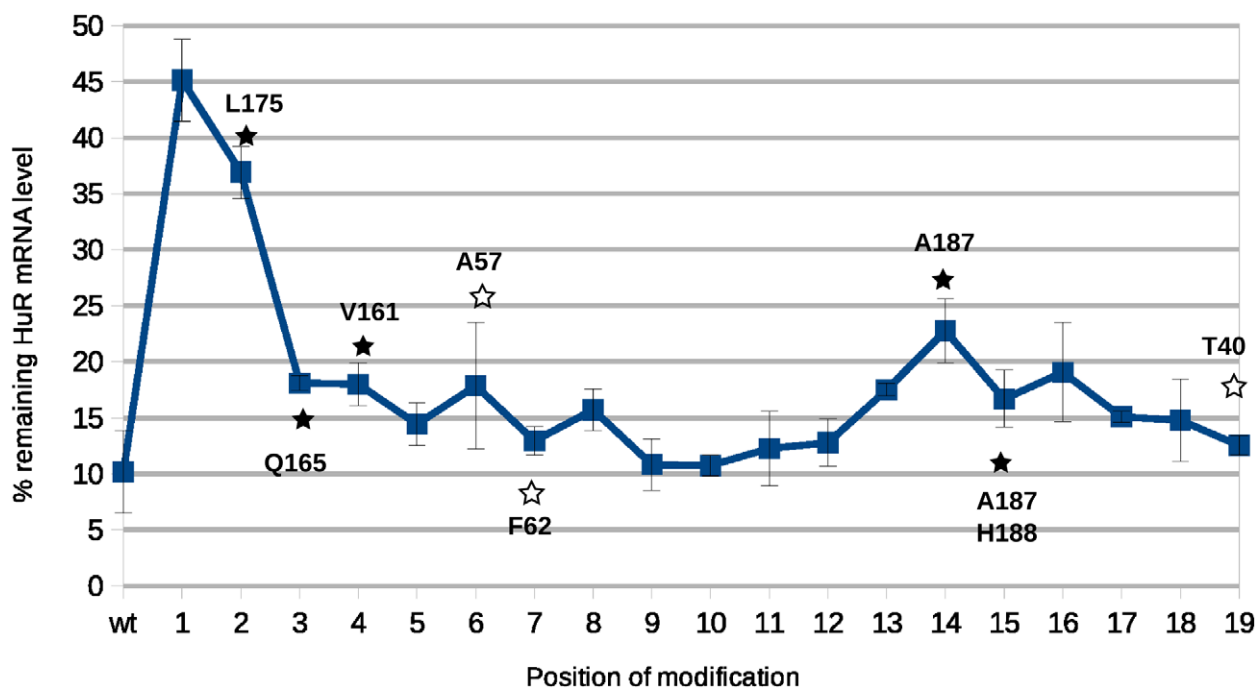


Figure EV5. Impact of EL86 (guide strand) 2'-MOE modifications on the knockdown efficiency of endogenous ELAVL1 mRNA in HeLa cells.

Remaining mRNA level (y-axis) was quantified by RT-qPCR (mean \pm SD from two replicates). The positions of the modified residues are shown on the x-axis. "wt" is the mRNA level quantified for unmodified EL86. Contacts between dsRBD12 and EL86 observed in our NMR structure (complex A) are shown with white (black) stars for those involving dsRBD1 (dsRBD2).